creative commons
COMMONS DEED

저작자표시-비영리-변경금지 2.0 대한민국

이용자는 아래의 조건을 따르는 경우에 한하여 자유롭게

- 이 저작물을 복제, 배포, 전송, 전시, 공연 및 방송할 수 있습니다.

다음과 같은 조건을 따라야 합니다:

저작자표시. 귀하는 원저작자를 표시하여야 합니다.

비영리. 귀하는 이 저작물을 영리 목적으로 이용할 수 없습니다.

변경금지. 귀하는 이 저작물을 개작, 변형 또는 가공할 수 없습니다.

- 귀하는, 이 저작물의 재이용이나 배포의 경우, 이 저작물에 적용된 이용허락조건을 명확하게 나타내어야 합니다.
- 저작권자로부터 별도의 허가를 받으면 이러한 조건들은 적용되지 않습니다.

저작권법에 따른 이용자의 권리는 위의 내용에 의하여 영향을 받지 않습니다.

이것은 이용허락규약(Legal Code)을 이해하기 쉽게 요약한 것입니다.

Disclaimer

dCollection

농학박사학위논문

Structural and Biochemical Analysis of Oxalate-Biosynthetic Components, ObcA and Obc1

옥살산 생합성에 관여하는 효소 ObcA 와 Obc1 의 구조와 생화학적 기능 분석

2017년 2월

서울대학교 대학원

농생명공학부 응용생명화학전공

오 준 택

A Dissertation for the Degree of Doctor of Philosophy

Structural and Biochemical Analysis of Oxalate-Biosynthetic Components, ObcA and Obc1

February 2017

Department of Agricultural Biotechnology

Seoul National University

Juntaek Oh

옥살산 생합성에 관여하는 효소 ObcA 와 Obc1 의 구조와 생화학적 기능 분석

Structural and Biochemical Analysis of Oxalate-Biosynthetic Components, ObcA and Obc1

지도교수 이 상 기

이 논문을 농학박사학위논문으로 제출함

2017 년 1 월

서울대학교 대학원

농생명공학부 응용생명화학전공

오 준 택

오준택의 박사학위논문을 인준함

2017 년 1 월

위 원 장 _____ (인)

부 위 원 장 _____ (인)

위 원 _____ (인)

위 원 _____ (인)

위 원 _____ (인)

Structural and Biochemical Analysis of Oxalate-Biosynthetic Components, ObcA and Obc1

Advisor: Sangkee Rhee

A Dissertation Submitted in Partial Fulfillment

of the Requirement for the Degree of

DOCTOR OF PHILOSOPHY

to the Faculty of

Department of Agricultural Biotechnology

at

SEOUL NATIONAL UNIVERSITY

by

Juntaek Oh

Date Approved

_____ _____

_____

_____

_____

_____

Abstract

In *Burkholderia* species, the quorum sensing-dependent production of oxalic acid is an indispensable process for bacterial growth during stationary phase. Oxalic acid produced plays a central role in maintaining the environmental pH, which counteracts inevitable population-collapsing alkaline toxicity in amino acid-based culture medium. In *B. glumae*, two enzymes are responsible for oxalic acid production. First, the oxalate biosynthetic component (Obc) A catalyzes the formation of a tetrahedral C6-CoA adduct from acetyl-CoA and oxaloacetate. Then the ObcB enzyme liberates three products from the C6-CoA adduct: oxalic acid, acetoacetate, and CoA. Interestingly, these two stepwise reactions are catalyzed by a single bifunctional enzyme, Obc1, from *B. thailandensis* and *B. pseudomallei*. Obc1 has an ObcA-like N-terminal domain and shows ObcB activity in its C-terminal domain, despite no sequence homology with ObcB. In this thesis, crystal structure and functional analysis of ObcA and Obc1 are reported, revealing structural and functional insights of oxalogenesis. Overall structure of ObcA and N-terminal domain of Obc1 exhibits $(\beta/\alpha)_8$-barrel fold, with a metal ion coordinated in its active site. In catalysis, substrate oxaloacetate serves as a nucleophile by forming an enolate intermediate mediated by Tyr residue as a general base, which then attacks the thioester carbonyl carbon of a second substrate acetyl-CoA to yield a tetrahedral adduct. In many reactions involving tetrahedral CoA intermediate, the presence of a negative charge in the intermediate leads to collapse of the intermediate, ejecting CoA moiety form the active site. However, the presence of the metal-coordination shell and absence of general acid(s) could produce an unusual

tetrahedral CoA adduct as a stable product. Structure of C-terminal domain of Obc1 has an α/β hydrolase fold that contains a catalytic triad for oxalic acid production and a novel oxyanion hole distinct from the canonical HGGG motif in other α/β hydrolases. Functional analyses through mutagenesis studies suggest that His934 is an additional catalytic acid/base for its lyase activity and liberates two additional products, acetoacetate and CoA. These results provide structural and functional insights into bacterial oxalogenesis; an example of the functional diversity of an enzyme to survive and adapt in the environment and divergent evolution of the α/β hydrolase fold, which has both hydrolase and lyase activity.

Keywords: Quorum sensing, Public goods, Oxalate biosynthetic component, Oxalic acid, Acetyl-CoA, Crystal structure, *Burkholderia* species

***Student Number*:** 2010-23457

Contents

List of Figures

Chapter I

Chapter II

Chapter III

List of Tables

List of Abbreviation

ObcA	oxalate biosynthetic component A
ObcB	oxalate biosynthetic component B
Obc1	oxalate biosynthetic component 1
CoA	coenzyme A
QS	quorum sensing
PCR	polymerase chain reaction
TEV	tobacco etch virus
IPTG	isopropyl β-D-L-thiogalactopyranoside
Tris	tris(hydroxymethyl)aminomethane
HEPES	4-(2-hydroxyethyl)-1-piperazineethanesulfonic acid
RMSD	root mean-square deviation
WT	wild-type
EDTA	ethylenediaminetetraacetic acid
DCPIP	2,6-dichlorophenolindophenol
SE	standard error
TCA cycle	tricarboxylic acid cycle

Chapter I.

Introduction

Bacterial quorum sensing

Bacterial quorum sensing (QS), a cell-to-cell communication process in many *Proteobacteria*, is mediated by small diffusible molecules called autoinducer and the receptor that can specifically bind to autoinducer (Fuqua and Greenberg, 2002, Miller and Bassler, 2001, Schuster et al., 2013, Waters and Bassler, 2005). Through quorum sensing, bacteria can monitor their own population density and behave as a group to adapt to a changing extracellular environment. Since the binding of an autoinducer to its receptor occurs only when a threshold concentration of the autoinducer is reached in the media, bacteria constantly produce and secrete autoinducers into their growth medium. However, at low cell density, dispersion of the autoinducer is dominant relative to its accumulation; therefore, binding does not occur (Fig. 1A). At high cell density, accumulation exceeds dispersion and the autoinducer begins to accumulate in the media. Once the concentration of the autoinducer crosses the threshold, the autoinducer binds to a specific receptor and the resulting complex controls the expression of genes involved in several population-wide characteristics, including bioluminescence, motility, and virulence-related factors (Fig. 1B) (Fuqua and Greenberg, 2002, Waters and Bassler, 2005). In this way, bacteria can act in a highly synchronized manner, as in a multicellular organism. This type of cooperation in an individual is very efficient when invading the host by secreting virulence factors or by eliminating competitors entering the growth medium through the biosynthesis of bactericidal molecules (Waters and Bassler, 2005). Bacteria also produce and secrete a wide range of chemicals or proteins that can be beneficial to their survival in different environments (Dandekar et al., 2012, Goo et al., 2015, Heilmann et al., 2015, Pai et al., 2012).

Figure 1. Bacterial quorum sensing and public goods.

(*A*) Bacteria continuously produce and secrete autoinducer molecules into growth medium. However, at low cell density, secreted autoinducer molecules are dispersed rather than accumulated; therefore, binding of the autoinducer to its receptor does not occur. (*B*) When a threshold concentration of the autoinducer is reached in the media, the autoinducer binds to a specific receptor and the resulting complex controls the expression of target genes. (*C*) One example of this phenomenon is public goods. In this case, the exoenzyme degrades an unusable complex nutrient to its usable form and acts as a public good. Although the quorum sensing-mediated expression of the exoenzyme is costly, the production of usable nutrients provides a direct benefit to the producer itself and to other group members in the medium, including exploiters who do not respond to quorum sensing.

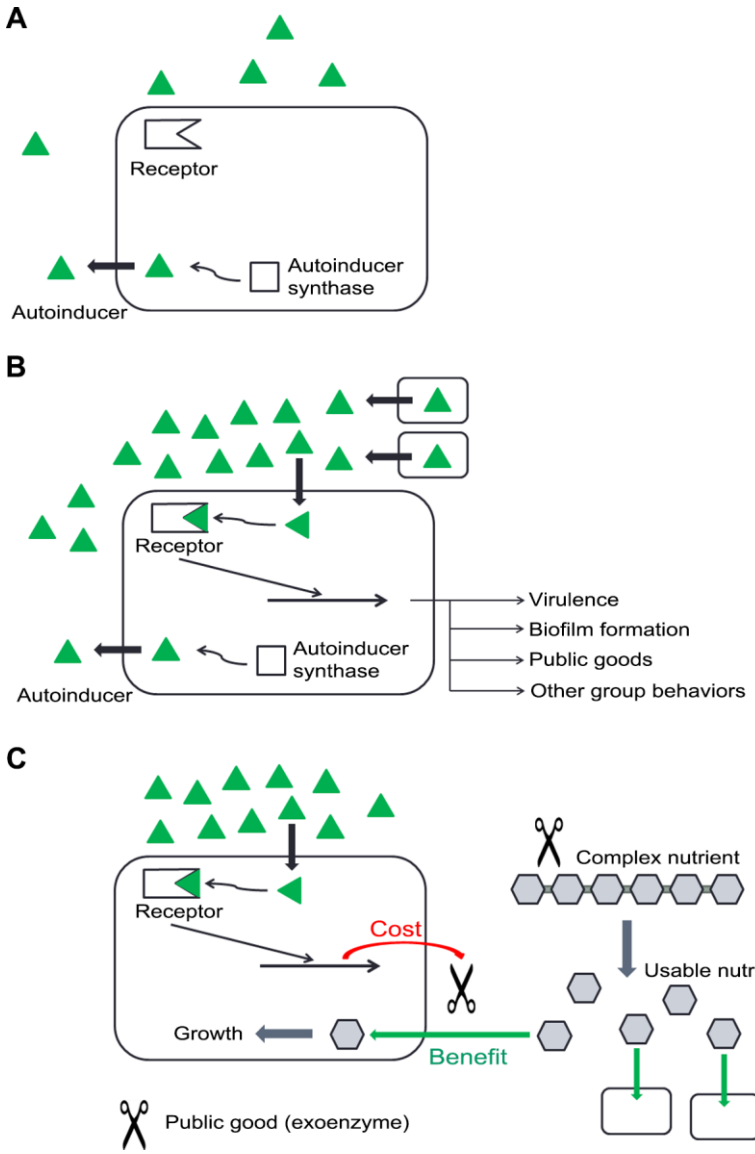
A
Receptor
Autoinducer synthase
Autoinducer
B
Receptor
Autoinducer synthase
Autoinducer
Virulence
Biofilm formation
Public goods
Other group behaviors
C
Receptor
Cost
Growth
Benefit
Public good (exoenzyme)
Complex nutrient
Usable nutrient

Public goods in bacteria

Recent studies on quorum sensing indicates that quorum sensing also regulates production of some molecules often referred to as ‘public goods’. Public goods provide a fitness advantage for the whole population, including individuals (i.e., exploiters) that lack the ability to synthesize these molecules. For example, public goods in a form of extracellular enzyme or small molecule play a role in nutrient acquisition, interspecies competition, and response to environmental change (Fig. 1C) (Dandekar et al., 2012, Diggle et al., 2007, Pai et al., 2012, Sandoz et al., 2007). Population density controls the production of public goods; this can be explained by comparing costs and benefits. Specifically, at low cell density, the majority of excreted public goods are dispersed before the molecules are utilized. This provides a small fitness benefit compared to the cost of producing the public goods. However, at high cell density, even if the producer of the public goods does not benefit directly, other bacteria in the growth medium can benefit from the public goods, thus providing a fitness benefit in terms of the whole population. Therefore, the production of public goods occurs cooperatively in a population-dependent manner by quorum sensing (Darch et al., 2012). Like most other living populations, pursuing the maximum benefit for individual bacteria does not always coincide with the best strategy for the bacterial community. Therefore, it is very interesting that evolution has selected cooperative individuals, even though there is the possibility of a ‘tragedy of commons’ arising from free riders who seek to exploit their profits without participating in quorum sensing. The quorum sensing-mediated production of ‘private goods’ could explain this observation (Dandekar et al., 2012).

Oxalic acid as a public good in *Burkholderia* species

In *Burkholderia* species, quorum sensing-mediated oxalogenesis is an indispensable cellular event for survival during the stationary growth phase. Specifically, *Burkholderia* species deficient in quorum sensing failed to proliferate in their population during stationary phase (Goo et al., 2015, Goo et al., 2012). Subsequently, it was found that those population collapse results from alkalization of growth medium. In rich growth medium, *Burkholderia* species utilizes amino acid as an primary carbon source, producing a large amount of ammonia. To counteract ammonia-mediated pH elevation, *Burkholderia* species have been evolved to produce and secrete oxalic acid, a highly acidic molecule that serves as a public good and plays a central role in maintaining pH homeostasis. Without oxalic acid, the whole population of *Burkholderia* species would collapse due to ammonia-mediated alkaline toxicity during the stationary growth phase.

Oxalic acid is ubiquitously present in humans, plants, as well as many bacteria and fungi. Its physiological roles are diverse, including the formation of calcium oxalate crystals for kidney stones in humans, calcium regulation in plants, and pathogenesis in fungi (Dutton and Evans, 1996, Franceschi and Nakata, 2005, Hoppe, 2012). However, a biochemical mechanism and pathway for endogenous oxalogenesis remains largely uncharacterized, although candidates for oxalate precursors include glyoxylate, glycolate, and glyoxal (Dutton and Evans, 1996, Franceschi and Nakata, 2005). Therefore, structural and functional interpretation of oxalic acid producing enzymes will provide molecular level of information about bacterial oxalogenesis.

Oxalate biosynthetic component in *Burkholderia* species

Quorum sensing-mediated production of oxalic acid is catalyzed by a two-step enzymatic reaction (Fig. 2A) (Li et al., 1999, Nakata and He, 2010). In *B. glumae*, two independent enzymes catalyze each step of reactions. The first enzyme, oxalate biosynthetic component (Obc) A, catalyzes the formation of a C6-CoA adduct, using acetyl-CoA and oxaloacetate as substrates. Substrate-labeling experiments further suggested that the C6-CoA adduct produced by ObcA differs regiochemically from the citroyl-CoA intermediate catalyzed by citrate synthase in the TCA cycle (Fig. 2B) (Li et al., 1999, Wiegand and Remington, 1986). Specifically, it has been suggested that, even though these two enzymes utilize identical substrates, the reaction mechanism may be completely different; to produce the citroyl-CoA intermediate, the acetyl moiety of acetyl-CoA should be deprotonated and attack the C2 carbon of oxaloacetate (Fig. 2B). However, in the ObcA-mediated reaction, the C3 carbon of oxaloacetate should be deprotonated and attack the thioester carbonyl carbon of acetyl-CoA (Fig. 2A). A second enzyme, ObcB, is responsible for the production of three different products, namely, oxalic acid, acetoacetate, and CoA. The C2-C3 and C4-S bonds in the C6-CoA adduct are cleaved by ObcB (Fig. 2A). Interestingly, in *B. thailandensis*, *B. pseudomallei* and *B. mallei*, the bifunctional enzyme Obc1 catalyzes these two reactions (Nakata, 2011). Given that Obc1 functionally complements ObcA and ObcB, it is not surprising that it contains activities of both enzymes. The N-terminal domain of Obc1 exhibits 52% identity with the amino acid sequence of ObcA (Fig. 3); however, the Obc1 C-terminal domain does not show any sequence homology with ObcB, even though it exhibits functional identity with ObcB (Nakata, 2011).

Figure 2. The overall reaction scheme of oxalogenesis in *Burkholderia* species.

(*A*) In *B. glumae*, the two enzymes ObcA and ObcB are involved in oxalogenesis, using acetyl-CoA and oxaloacetate as substrates, whereas in *B. thailandensis*, two domains in Obc1 mediate oxalogenesis. For convenience, atoms in oxaloacetate are colored according to the final products, and carbon atoms in the C6 moiety of the C6-CoA adduct are numbered. (*B*) In citrate synthesis, citrate is produced via the citroyl-CoA intermediate.

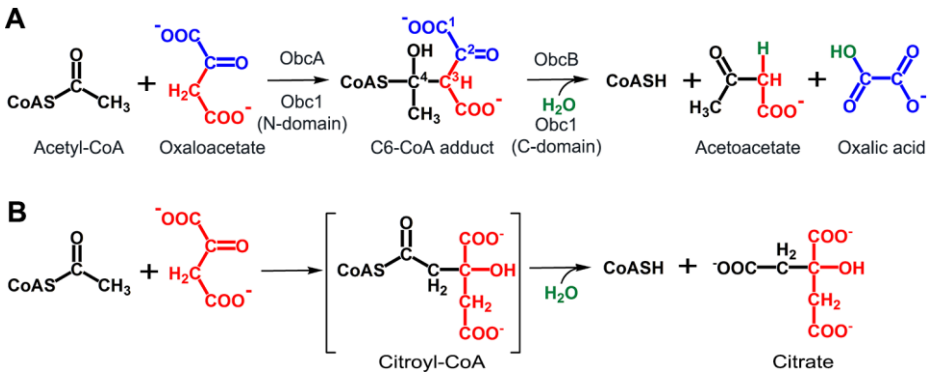
A
ObcA
Obc1
(N-domain)
ObcB
H2O
Obc1
(C-domain)
Acetyl-CoA
Oxaloacetate
C6-CoA adduct
Acetoacetate
Oxalic acid
B
Citroyl-CoA
Citrate

Figure 3. The sequence alignment of ObcA with its homologs.

The amino acid sequences of *B. glumae* ObcA (residues Met1 to Gly540; Gene Accession No. YP_002909440.1) are compared with other homologs, including those from *B. gladioli* (YP_004360639.1), *Pseudomonas putida* (ZP_19216180.1), *B. pseudomallei* (YP_111366.1), *B. mallei* (ZP_00438353.1), and *B. thailandensis* (ZP_02384435.1). Note that Obc1 from *B. thailandensis* is a bifunctional enzyme containing both ObcA and ObcB-like domains, and the identical enzymes were also identified from *B. pseudomallei* and *B. mallei*. Highly conserved residues are shown in red and boxed in blue, while strictly conserved residues are shown with a red background. Secondary structural elements defined in the apo form of ObcA are shown for the corresponding ObcA sequences with the cap and barrel domain in blue and black, respectively. Numbers in subscript represent additional structural elements in the corresponding region of a canonical $(\beta/\alpha)_8$-barrel fold, while cap domain structural elements are indicated with "C." Residues are indicated with different notations, including the metal-coordinating residues (diamond in cyan), ligand-interacting residues (triangle in green), and acetyl-CoA interacting residues (circle in gray); in particular, the general base Tyr322 is marked with a green asterisk. The sequence and structural alignment of C-domain of Obc1 is discussed ant presented at Fig. 18. This figure was prepared using ESPript (Gouet et al., 1999).

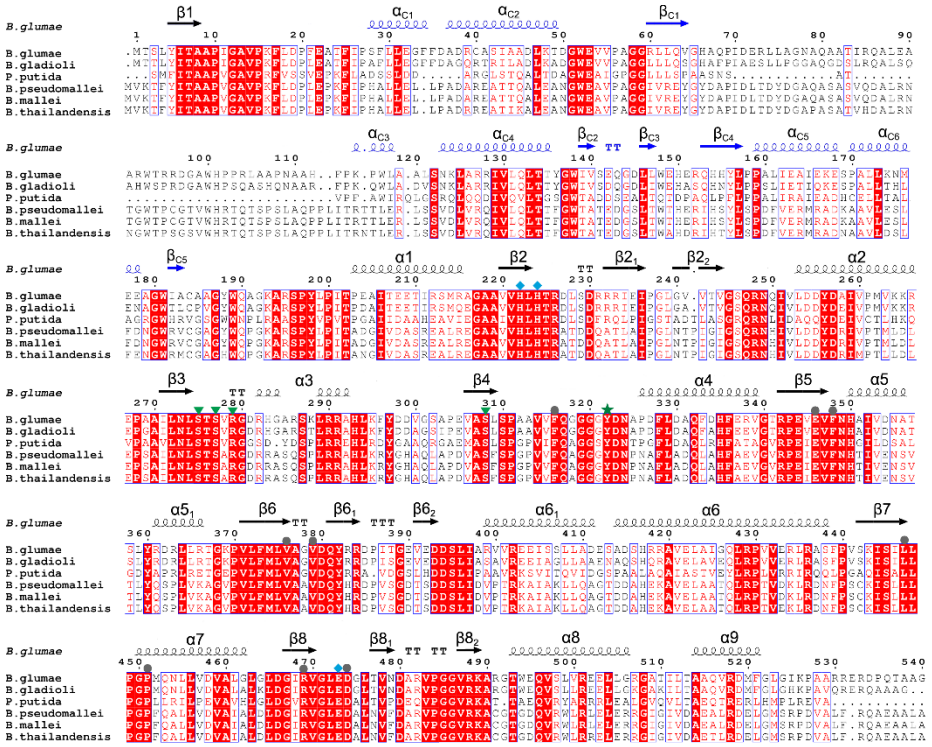
B.glumae
B.gladioli
P.putida
B.pseudomallei
B.mallei
B.thailandensis

Structural analysis of oxalate biosynthetic components

Many *Burkholderia* species are involved in plant or human pathogenesis. For example, *B. glumae* causes bacterial panicle blight in rice (Ham et al., 2011), while *B. cepacia* is an opportunistic pathogen in immunocompromised individuals, including those with cystic fibrosis and chronic granulomatous disease (Leitao et al., 2010). *B. pseudomallei* causes melioidosis, a lethal infection that leads to the formation of abscesses in internal organs (Galyov et al., 2010). Given that the quorum sensing dependent expression of oxalate biosynthetic components is an essential cellular event for bacterial proliferation during the stationary growth phase (Goo et al., 2012), understanding the molecular basis of these enzymes should provide the groundwork for the development of novel antibacterial agents for *Burkholderia* species.

In my thesis, crystal structure and functional analysis of ObcA and Obc1 will be discussed. Chapter II contain crystal structures of ObcA from *B. glumae*, including a ligand-free form and its complex with oxaloacetate and with a C4-CoA adduct and oxalate, the putative degratory products from the C6-CoA adduct. Structural analyses along with functional assays show that ObcA catalyzes its reaction in a unique manner relative to citrate synthase and other acetyl-CoA-dependent enzymes, providing structural insights into the first step in oxalogenesis and the mechanistic features of ObcA. In Chapter III, two different crystal structures of Obc1 are shown in its apo form and glycerol-bound form. Using structural and functional analyses, how Obc1 catalyzes the production of three different products is discussed. Together with structural study on ObcA, these observations provide structural insights into bacterial oxalogenesis.

Chapter II.

Structural and Functional Analysis of ObcA

Materials and Methods

ObcA purification

The gene for ObcA from *B. glumae* (Goo et al., 2012) was amplified by PCR with sequence-specific primers (Table 1). The resulting PCR product was subcloned into the NdeI and XhoI restriction sites of a modified pET28b expression vector (Merck) containing a TEV protease cleavage site at the junction between a His_5-tag and a multiple cloning site. The resulting plasmid was transformed into *Escherichia coli* BL21 (DE3). Cells were grown in Luria-Bertani medium at 37°C and when the optical density of the culture medium reached 0.7 at 600 nm, protein expression was induced by adding 0.5 mM of IPTG, followed by an additional 12–14 h of growth at 20°C. Cells were collected and sonicated in Buffer A containing 50 mM Tris (pH 8.0), 100 mM NaCl, and 5% (v/v) glycerol. The N-terminal His-tagged ObcA was purified using an immobilized metal affinity column (GE Healthcare) that had been equilibrated with Buffer A and then eluted with Buffer A containing additional 500 mM imidazole. The N-terminal His-tag of ObcA was subsequently removed by treatment of TEV protease overnight at 22°C, using a 20:1 molar ratio of ObcA to TEV protease. The resulting ObcA protein was further purified by immobilized metal affinity and size-exclusion chromatography using Superdex-200 (GE Healthcare) with Buffer A (Fig. 4).

For the structural determination of ligand-free ObcA, the N-terminal His-tagged seleno-L-methionine (SeMet)-substituted enzyme was expressed in *E. coli* B834 (DE3; Merck) using minimal medium supplemented with SeMet. The N-terminal His-tagged SeMet-ObcA was purified and the His-tag was

removed as described above. The purified SeMet-ObcA was further subjected to methylation of the lysine residues using established protocols (Walter et al., 2006). In brief, 2–5 mg/mL of SeMet-ObcA was subjected to the methylation reaction by adding the 50 mM of dimethylamine–borane complex and 80 mM of formaldehyde overnight at 4°C. To stop the reaction, 125 mM of Tris (pH 7.5) was added to reaction mixture. After centrifugation, the soluble fraction was further purified by size-exclusion chromatography using a Superdex 200 column (GE Healthcare) with Buffer A to remove any possible protein aggregates.

Table 1. Primers for ObcA and its mutants.

ObcA	
Forward	AGTCCATATGACATCGCTATACATCACG
Reverse	AGTCCTCGAGTCAGCCCGCCGCGGTC
R127A	GTCGAATAAACTGGCA**GCC**CGGATCGTGCTGCAA
R128A	GAATAAACTGGCACGC**GCG**ATCGTGCTGCAATTG
K193A	GGCAGGCCGGC**GCG**GCGCGTTCGCC
H222A	GCGGCGGTGGTG**GCT**CTGCACACGCG
H224A	CGGTGGTGCATCTG**GCC**ACGCGCGATCTCA
S275A	GATCCTGAACCTG**GCC**ACCAGCGTGCG
S277A	GAACCTGTCCACC**GCC**GTGCGCGGCGAC
R279K	CTGTCCACCAGCGTG**AAA**GGCGACCGCCACGGC
R279A	GTCCACCAGCGTG**GCC**GGCGACCGCCAC
S308A	CCGAGGTCGCC**GCG**CTGAGCCCG
F316A	CCGCGGTGGTG**GCC**CAGGGCGGCG
Y322F	GCGGCGGCGGC**TTC**GACAACGCGCC
Y322A	GGCGGCGGCGGC**GCC**GACAACGCGCC
E346A	GCGTCCCGAGGT**GGC**AGTGTTCAATCACG
F348A	CCCGAGGTGGAAGTG**GCC**AATCACGCGATCGT
V376A	GTTCATGCTG**GCG**GCGGGCGTCG
V379A	GGTGGCGGGC**GCC**GATCAATACCG
L447A	GAAGATCTCGATC**GCG**CTGCCGGGGCC
R469K	GGGCTCGACGGCATC**AAA**GTGGGGCTGGAGGAC
R469A	GCTCGACGGCATC**GCC**GTGGGGCTGGAG
E473A	GCGTGGGGCTG**GCG**GACGGCCTGAC
D474A	CGCGTGGGGCTGGAG**GCC**GGCCTGACCGTCAACG
Obc1	
Forward	CATATGCGCGAATACGGCTACGAC
Reverse	AAGCTTATGCGAGCGCTCGTCGCG
H227A	GGTGGTCCATCTG**GCC**ACGCGCGCGACC
Y326A	GGCGGGCGGCGGC**GCT**GACAACCCGAAC
E477A	CGCGTCGGCCTC**GCC**GACGCGCTGAACG

Sequences are described from 5’ to 3’. For mutagenic primers, only forward versions are listed. Underlined sequences indicate restriction sites used for cloning, and boldfaced-underlined sequences indicate mutated sequences.

Figure 4. Size-exclusion chromatography of ObcA.

Elution profile of size-exclusion chromatography for His-tag free ObcA. ObcA was eluted at 80.80 ml, which corresponds to 69.6 kD based on size marker. Given that the size of His-tag free ObcA is 59.3 kD, ObcA is estimated to be a monomeric protein.

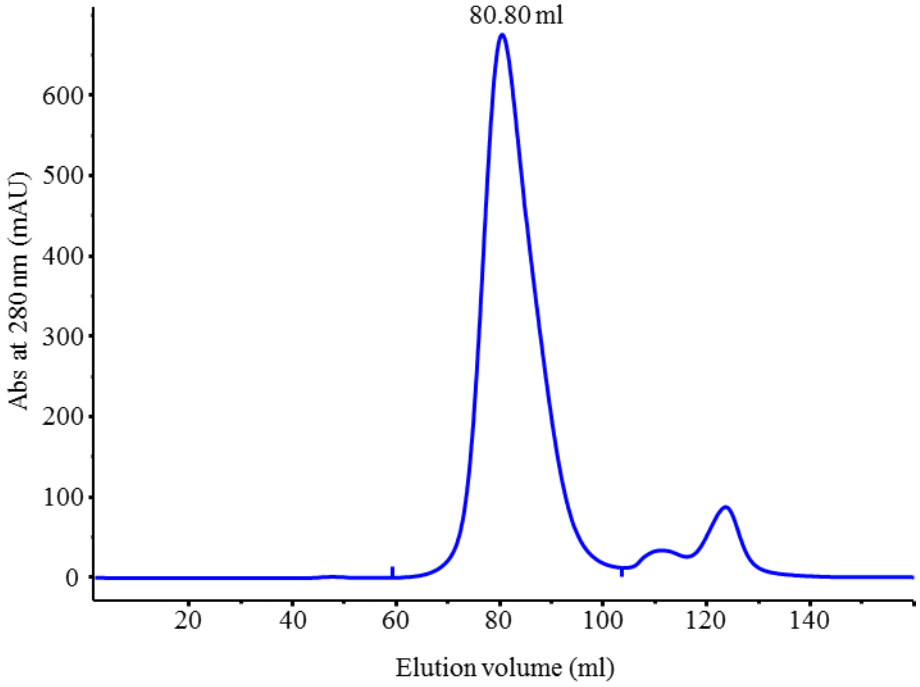
80.80 ml
Abs at 280 nm (mAU)
600
500
400
300
200
100
0
20
40
60
80
100
120
140
Elution volume (ml)

Crystallization and data collection

Crystallization was conducted at 22°C by a sitting drop vapor diffusion method using the native or the methylated SeMet-substituted ObcA (10–15 mg/mL). The presence of the Co^{2+} ion in the protein solution caused precipitation of ObcA or resulted in crystals diffracting only to a low resolution, although the Co^{2+} ion was the most effective metal ion for the enzyme catalysis (see below). Addition of one or both substrates was essential for the formation of crystals suitable for a high-resolution structure, but under my experimental conditions, the binding of the substrate(s) was not observed in the active site; however, a soaking experiment with the substrate(s) exhibited the binding of substrate(s) of interest. Therefore, crystallization for high-resolution structure analysis was performed using various combinations of ligand(s) and metal ions.

For the ligand-free ObcA, the methylated form of SeMet-substituted ObcA was initially crystallized with 2 mM acetyl-CoA under a crystallization solution of 0.1 M Tris (pH 8.0), 0.2 M $MgCl_2$, and 20% polyethylene glycol (PEG) 6000 (Fig. 5). Later, I collected higher-resolution data by soaking the crystal into the crystallization solution plus 100 mM CoA. To obtain an oxaloacetate-bound ObcA structure, the native ObcA crystal was soaked in the crystallization solution plus 20 mM oxaloacetate and 2 mM $MgCl_2$, after growing the crystal from 5 mM oxaloacetate and 1 mM CoA, with mother liquor containing 0.1 M HEPES (pH 7.5), 3% PEG 400, 2 M ammonium sulfate, 0.1 M $MgCl_2$, and 15% glycerol. The structure of ObcA in complex with the tetrahedral C4-CoA adduct was obtained using native ObcA. Specifically, the native ObcA crystal was produced by co-crystallizing ObcA with 15 mM acetyl-CoA, 20 mM oxaloacetate, and 1 mM $CoCl_2$ using a crystallization

buffer containing 0.2 M sodium/potassium tartrate, 0.1 M sodium citrate (pH 5.6), 2 M ammonium sulfate, and 15% glycerol. Prior to data collection, the crystal was soaked in a solution of 7.5 mM acetyl-CoA, 10 mM oxaloacetate, and 1 mM $CoCl_2$.

X-ray diffraction data were collected at 100 K with a 1-degree oscillation angle on beamline BL-1A at the Photon Factory (Japan) and 5C at the Pohang Accelerator Laboratory (Korea). Glycerol (15–20%) was used as the cryo-protectant in these experiments. Initially, multiwavelength anomalous dispersion data were collected at 2.8 Å using a crystal of the methylated SeMet-substituted ObcA. Subsequently, higher-resolution single-wavelength data became available for the 2.1 Å resolution ligand-free ObcA, the 2.0-Å resolution ObcA in complex with oxaloacetate, and the 2.28 Å resolution ObcA in complex with the C4-CoA adduct. The collected data were processed using the HKL2000 (Otwinowski and Minor, 1997), and all crystals had a space group of $P4_32_12$, with one monomer in the asymmetric unit, consistent with a size-exclusion chromatographic study demonstrating ObcA to be a monomeric protein (Fig. 4).

Figure 5. Crystal of SeMet-substituted ObcA.

Crystals were obtained under a crystallization solution of 0.1 M Tris (pH 8.5), 0.2 M $MgCl_2$, 20% PEG 6000, and 20% glycerol. Changing pH (8 to 8.5) and addition of 20% glycerol improved crystal size and shape.

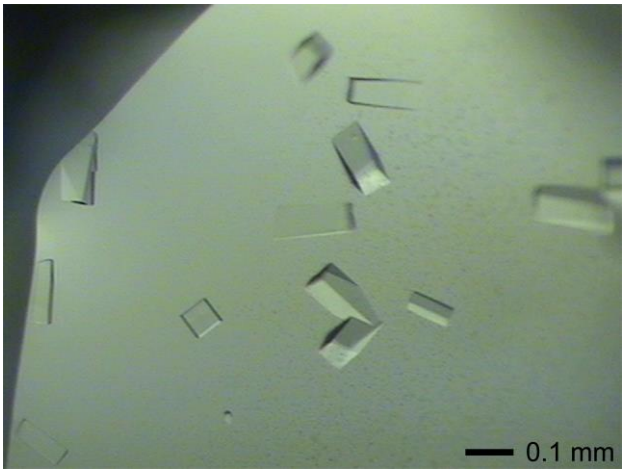
0.1 mm

Structure determination and refinement

The structure of the ligand-free ObcA was determined using the programs SOLVE (Terwilliger and Berendzen, 1999) and RESOLVE (Terwilliger, 2000), with multiwavelength anomalous dispersion data at 2.8 Å resolution. The model was built and refined using the programs COOT (Emsley et al., 2010) and PHENIX (Adams et al., 2010). After several cycles of manual inspection and refinement, residues ranging from Thr2 to Ile525 were located, except for the highly disordered region of Asp71 to Ala91 and Arg96 to Trp100. The model was then refined against the 2.1 Å resolution data available. During assignment of water molecules in the structure, I noticed the presence of a metal ion, based on strong density from the *Fo–Fc* electron density map, as well as its geometry to the nearby residues and other water molecules. I assigned the metal ion as a Mg^{2+} ion because the crystallization solution contained 0.2 M $MgCl_2$. The structure for a ligand-free ObcA was used as the starting model for determining a structure of the oxaloacetate-bound ObcA. In the middle of refinement, the *Fo–Fc* electron density map showed that oxaloacetate was bound to the metal-binding site. Similarly, the structure of ObcA in complex with the tetrahedral C4-CoA adduct and oxalate was determined. In particular, the *Fo–Fc* electron density map corresponding to the tetrahedral C4-CoA adduct and oxalate was evident. Although initially modeled as a Mg^{2+} ion, the metal ion was found to correspond to a Co^{2+} ion due to its presence in the soaking solution and the strong residual density from the *Fo–Fc* electron density map. Details for the data collected and refinement are listed in Table 2.

Table 2. ObcA data collection and refinement statistics.

Data set	Ligand-free	Oxalo-acetate	C4-CoA adduct	Ligand-free		
PDB ID	4NNA	4NNB	4NNC			
Crystal	Methylated SeMet	Native	Native	Methylated SeMet	Methylated SeMet	Methylated SeMet
Wavelength (Å)	0.97935	0.97948	0.97948	0.97935 Peak	0.97957 Edge	0.97167 Remote
Resolution (Å)	50-2.1 (2.18-2.10)[a]	50-2.0 (2.07-2.00)	50-2.28 (2.36-2.28)	50-2.8 (2.90-2.80)	50-2.8 (2.90-2.80)	50-2.8 (2.90-2.80)
Unique reflections	40015	49954	33093	19639	19631	19912
Multiplicity	13.7(14.5)	9.5(9.8)	9.4(9.4)	13.4(13.2)	13.4(13.2)	13.5(13.1)
R-merge (%)	18.0(59.3)	12.1(49.5)	15.0(94.9)	13.1(51.4)	12.3(50.4)	13.5(62.4)
Completeness (%)	95.9(99.8)	96.2(100)	99.6(98.8)	99.8(100)	99.7(100)	99.9(100)
Mean I/sigma(I)	12.1(5.0)	13.3(4.7)	11.4(2.8)	21.4(5.7)	24.2(6.1)	22.2(4.9)
Wilson B-factor	27.65	30.56	32.93			
Space group	$P4_32_12$					
Unit Cell (Å)						
a=b, c	173.5, 46.2	177.0, 47.8	174.6, 46.1	178.2, 48.2	178.2, 48.2	178.2, 48.2
$\alpha = \beta = \gamma$	90					
Refinement						
R work[b] (%)	19.8	21.0	20.2			
R free[c] (%)	23.7	24.6	23.5			
No. of atoms	4270	4056	3937			
Protein	3867	3741	3731			
Ligands	1	10	62			
Waters	402	305	144			
Protein residues[d]	498	484	483			
RMS (bonds)	0.007	0.007	0.008			
RMS (angles)	1.08	1.09	1.13			
Ramachandran favored (%)	97	96	96			
Ramachandran outliers[e] (%)	0	0	0.21			
Clashscore	2.45	2.93	2.78			
Average B-factor	29.8	35.5	32.4			
Protein	29.3	35.3	32.1			
Ligands	19.1	30.5	50.0			
Waters	34.7	38.2	31.8			

[a]Numbers in parentheses refer to data in the highest resolution shell.

[b]$R_{work} = \Sigma \, ||F_{obs}|-k|F_{cal}||/ \Sigma|F_{obs}|$

[c]R_{free} is the same as R_{obs} for a selected subset (10%) of the reflections that was not included in prior refinement calculations.

[d]Ordered residues: ligand-free structure (Thr2 to Ile70 and Arg92 to Arg95 and His101 to Ile525), oxaloacetate bound structure (Thr2 to Ile70 and Ala111 to Ile525), and a C4-CoA adduct bound structure (Thr2 to Ile70 and Ala110 to Ala523).

[e]Two outliers identified in C4-CoA adduct bound complex, Ser358 and Gly450.

Purification of Obc1* and various ObcA mutants

For the assay, the WT and mutant ObcA enzymes were expressed as described above. I also used a mutant enzyme of a bifunctional Obc1 from *B. thailandensis* (hereafter indicated as Obc1*) to replace the function of ObcB in the reaction due to an issue with solubility associated with *B. glumae* ObcB. Genes for the mutant ObcA and Obc1* were constructed by site-directed mutagenesis using mutagenic primers (Table 1). The N-terminal His-tagged enzyme was purified by immobilized metal affinity chromatography followed by a desalting step using a column of HiPrep 26/10 (GE Healthcare) and a buffer solution containing 50 mM Tris (pH 8.0), 100 mM NaCl, and 5% (v/v) glycerol for various ObcA mutants or 50 mM HEPES (pH 7.0), 300 mM NaCl, and 5% (v/v) glycerol for Obc1*. The enzymes were used without removing the His-tag. For measurement of the metal-dependent activity, purified WT ObcA and Obc1* enzymes were dialyzed against Buffer A plus an additional 10 mM EDTA and subsequently against an EDTA-free buffer A. Absence of metal ions, including Co^{2+}, Mn^{2+}, Ni^{2+}, or Mg^{2+}, in ObcA was further validated by inductively coupled plasma atomic emission spectroscopy analysis.

Activity assay of ObcA

An enzyme activity assay was performed using two different methods, each measuring a different product. First, a steady-state kinetic analysis for ObcA was carried out by monitoring the time-dependent production of free CoA using DCPIP, a dye that reacts with the sulfhydryl group of CoA to causes a linear decrease in absorbance at 600 nm (Raychaudhuri et al., 2005). In a second assay, total oxalic acid produced was measured using an oxalate kit (Trinity Biotech).

To monitor the production of free CoA, enzyme assays were performed at 30°C using a UV-visible spectrophotometer (Jasco). The reaction mixture includes 50 mM Tris buffer (pH 8.0), 100 mM NaCl, 100 μM DCPIP, 100 μM $CoCl_2$, and 400–800 μM acetyl-CoA. The mixture was incubated for 20 min at 30°C, followed by the addition of 50–500 nM WT ObcA or its mutant and 800 nM Obc1*, after which the mixture was incubated for an additional 4 min. Enzyme reaction was initiated by adding 1–10 mM oxaloacetate to the resulting reaction mixture, and the initial velocity was determined by measuring the linear decrease in absorbance at 600 nm from the time range of 60 to 105 s; nonlinear decreases in absorbance were observed in the first 60 s. The 800 nM Obc1* was confirmed as the saturating concentration for the coupled reaction of a steady-state kinetic assay for ObcA. Free CoA concentration produced per minute was calculated from the standard reaction curve. Specifically, the initial velocity as a function of free CoA concentration was obtained using my assay mixture but in the absence of enzymes and substrates. The K_M and V_{max} values were obtained using SigmaPlot, and k_{cat} values were computed by dividing V_{max} by the ObcA concentration used.

Total oxalic acid production was measured following the manufacturer's

protocol. The enzyme reaction was also conducted at 30°C, and the reaction mixture was identical with that in the first method, except for DCPIP, which contained 50 mM Tris buffer (pH 8.0), 100 mM NaCl, 100 μM $CoCl_2$, 400 μM acetyl-CoA, and 1 mM oxaloacetate. The assay solution containing both substrates was incubated for 1 min, and then 50 nM ObcA or its mutant enzyme and 800 nM Obc1* were added to the mixture, incubating for another 5 min. I found that 5 min is sufficient to complete the reaction when using WT ObcA. After the ObcA and Obc1* reactions, 30 μL of the resulting reaction mixture was added to 660 μL of the assay reagent from the manufacturer, and the absorbance at 590 nm was measured after 5 min. Total oxalic acid produced was calculated from the standard curve. Specifically, the standard curve as a function of oxalic acid concentration was obtained in the absence of two enzymes and two substrates.

Results

Structure of ObcA in the ligand-free form

ObcA (residues Thr2 to Ile525) consists of two structurally distinct domains: a small cap and a large barrel domain (Figs. 3 and 6A). The overall structure comprises a $(\beta/\alpha)_8$-barrel fold with the cap domain (Pro15 to Tyr198) inserted into a loop between β1 and α1 of the barrel fold (Fig. 6B). This topology represents a unique structural architecture. Homologous structure searches using DALI (Holm and Rosenstrom, 2010) indicated that despite the abundance of $(\beta/\alpha)_8$-barrel folds in the Protein Data Bank, no other structures resemble the overall features of ObcA. In particular, DALI search using the cap domain indicates that the most homologous structure found exhibits a Z-score of only 1.3. The N-terminal 14 residues form β1 in the barrel fold. Other insertions occur in the loop regions of the barrel domain, specifically in the loops following β2, β6, and β8 (Figs. 3 and 6B). First, two long antiparallel β-strands ($\beta2_1$ and $\beta2_2$) following β2 protrude vertically from the barrel domain and belong structurally to the cap domain (hereafter, subscripts used in this manuscript represent additional structural elements present in the corresponding region of the canonical $(\beta/\alpha)_8$-barrel fold, and the cap domain structural elements are indicated by "C"). The second insertion consists of two β-strands and one α-helix inserted into the loop connecting β6 and α6. The resulting antiparallel β-strands ($\beta6_1$ and $\beta6_2$) protrude horizontally from the barrel, and the $\alpha6_1$ is packed in an antiparallel orientation to the N-terminal region of α6. Additional alterations are seen in a loop following β8, in which two antiparallel β-strands ($\beta8_1$ and $\beta8_2$) project horizontally from the barrel. In

the successive α8, a loop runs through the bottom of the barrel, and the C-terminal α9 turns nearly 90° relative to the preceding loop, thus sealing off any possible opening in the bottom of the barrel fold. In addition to these obvious modifications, an additional helix $\alpha5_1$ exists between α5 and β6.

The cap domain is located along the C-terminal ends of the central β-strands in the barrel fold. It does not share any structural similarity with the known folds and consists of two segments (Fig. 6A). In one segment, two antiparallel β-strands ($\beta2_1$ and $\beta2_2$) from the barrel domain and three twisted β-strands (β_{C5}, β_{C1}, and β_{C4}) are arranged perpendicularly along the long axis of the strands, with two helices (α_{C1} and α_{C2}) filling the open space between them. In the second segment, a layer of helices and β-strands is packed on the other side of the three twisted β-strands from the first segment, forming a funnel-shaped fold. The potential small opening in the funnel-like structure is located toward the barrel domain but completely occluded by two β-strands ($\beta8_1$ and $\beta8_2$) from the barrel fold, while the larger opening at the opposite end comprises a highly disordered region.

Figure 6. The overall structure and topology of ObcA.

(*A*) The overall structure of ObcA in a ligand-free form is displayed, indicating an cap domain (blue) and a C-terminal $(\beta/\alpha)_8$-barrel fold (magenta). Additional structural elements from the barrel domain (green), β1 (yellow), and a metal ion (green sphere) are also indicated. (*B*) The topology of ObcA is shown with color coding identical to that described in (*A*). The C-terminus of β_{C1} to the N-terminus of α_{C3} is highly disordered and not modeled. Those termini are marked with a black dot. Secondary structure elements are shown in Fig. 3.

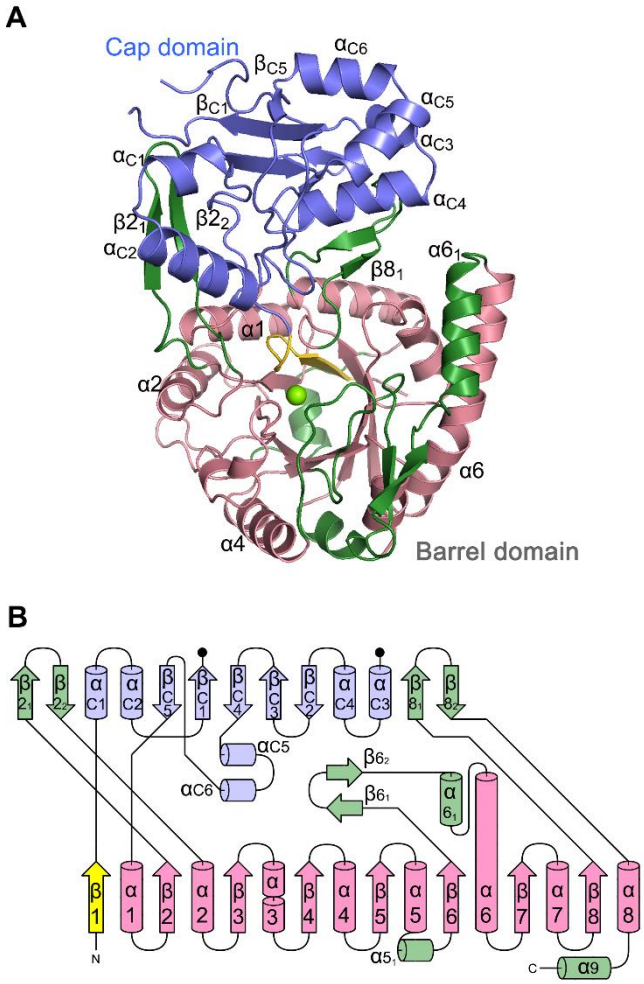
A
Cap domain
αC6
βC5
βC1
αC5
αC3
αC1
αC4
β2₁
β2₂
αC2
α6₁
β8₁
α1
α2
α6
α4
Barrel domain
B
αC5
αC6
β6₂
β6₁
α6₁
N
α5₁
C
α9

The active site in ligand-free ObcA

The putative active site of ObcA was indicated by the presence of a metal-binding site in a cavity of the C-terminal barrel fold, consistent with a previous observation that ObcA activity requires a metal ion (Li et al., 1999). My functional analysis also provided evidence for a metal-dependent activity of ObcA, in which the Co^{2+} ion is the strongest (see below). Given that purified ObcA does not contain metal ions characterized by inductively coupled plasma atomic emission spectroscopy analysis and that the crystallization condition of a ligand-free ObcA requires 200 mM Mg^{2+}, the metal-binding site identified in a ligand-free ObcA is likely occupied by the Mg^{2+} ion. The active site is ~20 Å from the surface of the enzyme (Fig. 7, A and B). Three residues, including His222 and His224 in β2, and Glu473 in the loop of β8, along with three water molecules, ligate the metal ion, representing an octahedral coordination (Fig. 7C). In particular, His224 and Glu473, as well as two water molecules spanning these residues, form a square coordination for the equatorial plane, while His222 in the interior floor of the cavity and a water molecule proximal to the surface of the enzyme represent the axial ligands. Arg279 on the tip of the loop following β3 covers the metal-binding site, but the electron density for the loop, particularly Arg279 to Gly284, is relatively disordered, suggesting dynamic features of the loop. Many residues are present in the vicinity of the metal-coordinating ligands. In particular, water molecules present in the shell are within a hydrogen bonding distance from the nearby residues, including Ser275 and Ser308, for one *trans* to Glu473, and Arg469 for a water molecule across from His224 (Fig. 7D).

Noticeably, a relatively large pocket remained vacant, located adjacent to

the metal-binding site and extending from the active site cavity into the enzyme surface along the central β-strands of the barrel fold (Fig. 7, A and B). Most pocket-forming residues are more than 4.5 Å distant from the equatorial water molecule *trans* to His224, and the wall of the pocket is lined with three ladders of residues: Glu346 and Arg469 constituted the bottom floor, and the second ladder consisted of Asp474, Phe348, Val376, and Leu447, while the rim of the pocket on the surface involved Phe316, Val379, and Pro449. Among those residues, the innermost residue Arg469 is within a hydrogen bonding distance from the equatorial water molecule.

Figure 7. The active site of ObcA in a ligand-free form.

(*A*) The active site is shown for ObcA in a ligand-free form with the nearby residues. Acetyl-CoA-interacting residues are indicated in gray, while metal-ligating and oxaloacetate-interacting residues (defined later) are colored in cyan. An octahedral geometry of the metal-coordinating shell is presented. Metal-coordinating water molecules (red sphere) and the metal ion (green sphere) are also indicated. (*B*) The cavity of the active site of ObcA is shown as surface representation in a ligand-free form, with the cap domain (blue) and barrel domain (gray). Water molecules in the metal-coordinating shell are indicated with red spheres. (*C*) The metal-coordinating shell is presented, with water molecules and metal ions overlaid with an *Fo–Fc* map (4σ). (*D*) A schematic drawing is presented for the interactions in the active site of ObcA in the ligand-free form. Dashed lines indicate possible hydrogen bonds within an interatomic distance of 3.6 Å. Note that Glu346 is 3.8 Å apart from the water molecule.

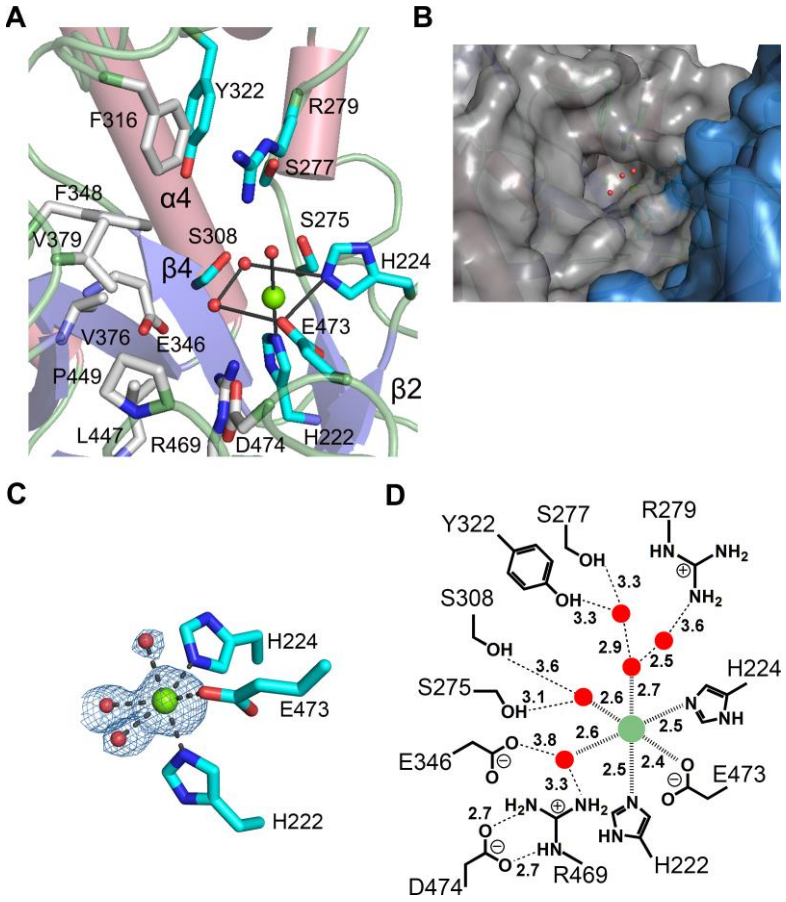
A
Y322
F316
R279
S277
α4
F348
S275
V379
S308
β4
H224
E473
V376
E346
P449
β2
L447
R469
D474
H222
B
C
H224
E473
H222
D
Y322
S277
R279
S308
H224
S275
E346
E473
H222
D474
R469

Structure of ObcA in complex with oxaloacetate

The structure of ObcA in complex with oxaloacetate shows that oxaloacetate is identified in the metal-binding site, with its oxalo group pointing toward Arg279 (Fig. 8A). The binding of oxaloacetate caused no noticeable change in conformation, relative to a ligand-free ObcA, with an RMSD of 0.41 Å for 484 Cα atoms. Specifically, the C4 carboxylate of oxaloacetate replaced the metal-ligating water molecule *trans* to Glu473 in the ligand-free ObcA, and the O2 atom in the oxalo group occupied the sixth coordination. The water molecule across from His224 is still present in the shell, maintaining its interaction with active site residues apparent in a ligand-free ObcA. Thus, the resulting interactions represent a typical octahedral coordination to the bound metal. The two carboxylates of oxaloacetate are stabilized by the nearby residues, including Ser277, Arg279, and Tyr322 for the C1 carboxylate, and Ser275 and Ser308 for the C4 carboxylate.

In addition to these nearby active site residues, possibly facilitating the binding of oxaloacetate, Tyr322 was brought into the immediate vicinity of the substrate, and the side chain hydroxyl group was placed ~3.3 Å distant from the C3 carbon of oxaloacetate (Fig. 8, A and B). In particular, its configuration fulfills the stereochemical requirements of an in-line projection to abstract a proton from the C3 methylene group, with an angle of 109° connecting the OH group in Tyr322, and C3 and C4 atoms of oxaloacetate. The binding of oxaloacetate stabilized the loop covering the metal-binding site, presenting a well-defined interaction between Arg279 and the C1 carboxylate of oxaloacetate. The pocket adjacent to the metal-coordinating shell exhibited no major changes, with the exception that the side chain of Glu346 was closer to

a metal-ligating water molecule across from His224 (Figs. 7D and 8B).

Figure 8. The active site of ObcA in an oxaloacetate bound form.

(*A*) The stereoview of the active site of ObcA in complex with oxaloacetate (yellow) is shown. The dashed line between Try322 and the C3 group of oxaloacetate does not represent a hydrogen bond. (*B*) The respective interactions are displayed. Dashed lines with an interatomic distance indicate possible hydrogen bonds. Oxaloacetate in the right of (*B*) is overlaid with an *Fo–Fc* map contoured at 2.3 σ.

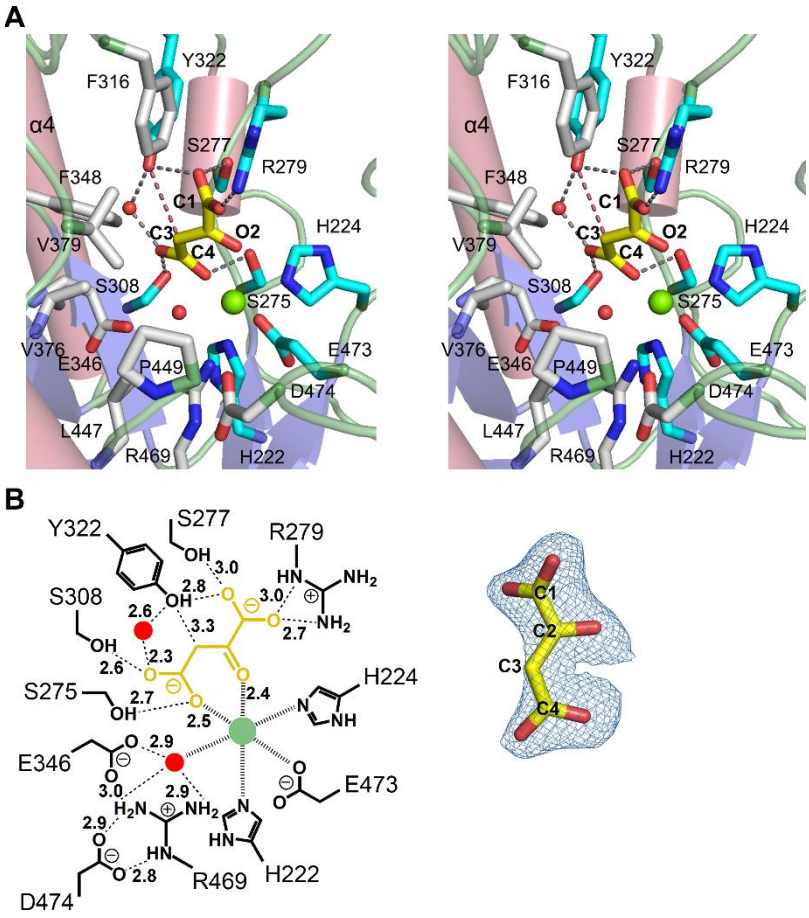
A
Y322
F316
α4
S277
R279
F348
C1
C3
O2
H224
V379
C4
S308
S275
V376
E346
P449
E473
D474
L447
R469
H222
B
Y322
S277
R279
S308
H224
S275
E346
E473
R469
H222
D474
C1
C2
C3
C4

Structure of ObcA in complex with the bisubstrate adduct

I unexpectedly identified a C4-CoA adduct and oxalate in the active site of ObcA at 2.28 Å resolution (Fig. 9). The electron density map in the active site indicated that it does not represent an authentic C6-CoA adduct as I had anticipated. Rather, the density was separated into two segments, one for a C4-CoA adduct lacking the oxalo group in the oxaloacetate moiety and a second one for oxalate (Figs. 10-12). Given that all three products, including oxalic acid, acetoacetate, and CoA, are readily produced only in ObcB-dependent reactions (Nakata and He, 2010), it is highly likely that under my experimental conditions, the oxalo group was spontaneously released from a C6-CoA adduct, forming oxalate, which was then trapped within the active site. Consistent with this crystallographic observation, my activity assay in solution indicate that oxalate is very slowly and spontaneously produced in an ObcA-dependent manner (Fig. 13A). Previous study on ObcA also supports spontaneous production of oxalic acid (Nakata and He, 2010). Therefore, I conclude that the C4-CoA adduct and oxalate are degradation products from the C6-CoA adduct, a proposed ObcA product (Fig. 2A).

The structure of ObcA in complex with a C4-CoA adduct and oxalate is almost identical with a ligand-free ObcA, with an RMSD of 0.40 Å for 483 Cα atoms. The resulting C4-CoA adduct and oxalate occupy the metal-coordinating shell and its nearby pocket (Fig. 10B). The phosphopantetheine arm of the adduct is positioned in the pocket along the central β-strands of the barrel domain. Specifically, this arm is bound to a concave region between the cap and barrel domain composed of three different loops following β1, β7, and β8 in the barrel fold. This region was filled with a string of water molecules in the

oxaloacetate-bound ObcA complex. Several positively charged residues, such as Arg127, Arg128, Lys193, and Lys489, are localized around the phosphate group of the arm (Fig. 10C). Noticeably, the side chain of Lys193 underwent large changes that prompted its interaction with the phosphate group, while the 3'-phosphoadenosine monophosphate moiety interacted with few residues (Fig. 11). In contrast, oxalate is located near the C4-CoA adduct (Figs. 9 and 12, A and B), and its binding site is almost identical to the oxalo group in the oxaloacetate-bound ObcA but with a different orientation (Fig. 12C). As a result, oxalate is at least 2.6 Å away from the C4-CoA adduct. One carboxylate present in oxalate is within hydrogen bonding distance to Ser277 and Tyr322, as I observed in the oxaloacetate-bound ObcA (Fig. 8A), while the other carboxylate is nearly in the same position with the O2 atom present in oxaloacetate, occupying a position for the axial water molecule in a metal-coordinating shell (Fig. 11).

Notable features exist in the C4-CoA adduct. The carbon atom adjoined to the sulfhydryl group of CoA is in the tetrahedral configuration (Fig. 12B). The resulting tetrahedral C4-CoA adduct therefore consists of acetoacetate and CoA moieties (Fig. 2A), consistent with the observation that acetoacetate and free CoA moieties comprise the two other products in ObcB-dependent reactions. However, the adduct differs in chemical structure from a cognate acetoacetyl-CoA containing a thioester linkage between the sulfhydryl group of CoA and the carboxylate of acetoacetate. The acetoacetate moiety of the C4-CoA adduct occupies two adjacent positions in the equatorial plane of the metal coordination shell (Figs. 9 and 11). The carboxylate in the adduct replaced the C4 carboxylate position of oxaloacetate, while the oxygen atom on the

tetrahedral carbon occupied a position for the water molecule *trans* to His224. The resulting geometry around the metal ion is essentially identical with those of the ligand-free and oxaloacetate-bound ObcA. The binding of the phosphopantetheine arm was further stabilized by interactions with the pocket residues, for example, the Arg469 interaction with the oxygen atom in the adduct's tetrahedral carbon, the Asp474 and Arg279 interactions with the arm of the adduct, and many other hydrophobic interactions.

Taken altogether, it is concluded that ObcA catalyzes the formation of a C6-CoA adduct by joining the oxaloacetate C3 carbon to the thioester carbonyl carbon of acetyl-CoA, resulting in a tetrahedral C6-CoA adduct, which in turn serves as a substrate for ObcB in the production of oxalic acid, acetoacetate, and CoA. Identification of a tetrahedral C4-CoA adduct in this study is unusual, considering that the tetrahedral CoA is thought to be a reaction intermediate in many CoA-dependent reactions, subsequently collapsing into a free CoA by protonating the leaving CoA thiolate anion (Dyda et al., 2000). In contrast, the presence of the tetrahedral C4-CoA adduct in ObcA is made possible by the fact that no obvious candidates for general acid(s) are positioned around the sulfur atom of the adduct in ObcA. Further inspection of the adduct interacting residues suggests that the oxygen atom on the tetrahedral carbon is possibly in a hydroxyl form rather than a labile anionic form, providing a structural foundation for the stability of the tetrahedral adduct. Specifically, the nearby Arg469, which is located within a hydrogen bonding distance from hydroxyl group of the adduct, likely protonates the oxygen atom on the tetrahedral carbon (Figs. 9 and 11; see Discussion). Identification of a bisubstrate adduct in the active site also suggests that the reaction proceeds via a ternary complex

mechanism requiring the binding of both substrates prior to catalysis.

Figure 9. The binding mode of the C4-CoA adduct and oxalate.

The stereoview of the active site is shown for ObcA in complex with the bisubstrate C4-CoA adduct (green) and oxalate (yellow), noting a tetrahedral carbon (black asterisk) and Co^{2+} ion (black sphere). Dashed lines are potential hydrogen bonds within an interatomic distance of 3.5 Å, and the schematic drawing for these interactions is shown in Fig. 11.

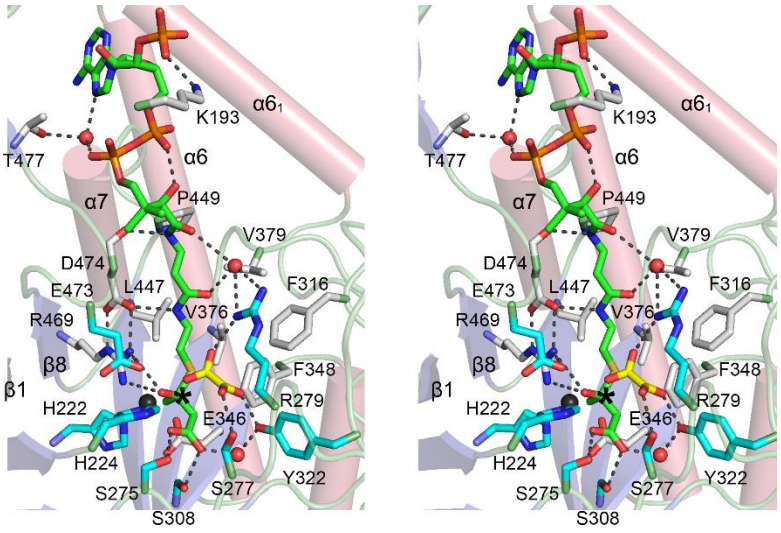
α6₁
K193
T477
α6
α7
P449
V379
D474
E473
L447
F316
R469
V376
β8
F348
β1
H222
R279
E346
H224
Y322
S275
S277
S308
α6₁
K193
T477
α6
α7
P449
V379
D474
E473
L447
F316
R469
V376
β8
F348
β1
H222
R279
E346
H224
Y322
S275
S277
S308

Figure 10. The electron density map and binding pocket of the C4-CoA adduct and oxalate.

(*A*) The model for the C4-CoA adduct, oxalate, and Co^{2+} is overlaid with an *Fo–Fc* electron density map at 2.3 σ. (*B*) The binding cavity of the C4-CoA adduct and oxalate is displayed in a surface representation of ObcA, with the metal ion indicated in gray. (*C*) The surface charge distribution of the adduct-binding region is shown in an orientation similar to Fig. 7C. Positive and negative charge distribution is indicted in blue and red, respectively. Note that the adenosine 3', 5'-diphosphate moiety is placed in the vicinity of the positive charge.

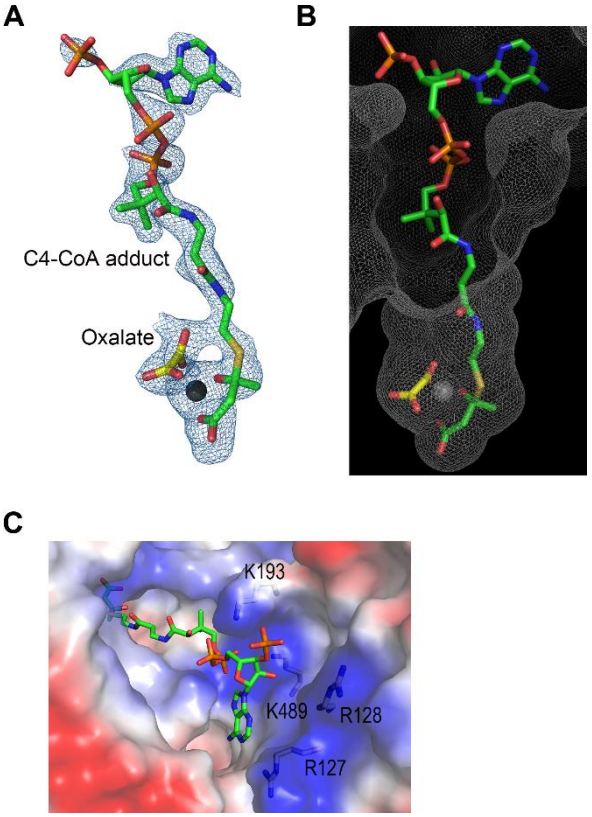
A
B
C4-CoA adduct
Oxalate
C
K193
K489
R128
R127

Figure 11. The schematic representation of a C4-CoA adduct and oxalate in the active site of ObcA.

A schematic representation is shown for the interactions in the active site of the ObcA complexed with the C4-CoA adduct and oxalate. Dashed lines indicate possible hydrogen bonds within an interatomic distance of 3.5 Å among the metal-coordinating shell, ligand, and the nearby residues. Interaction distances between Lys489 and the phosphate and between Arg279 and the adduct are 3.8 and 3.6 Å, respectively. Many residues are within close enough distance to allow for hydrophobic interactions. Note that only a few interactions are identified in the vicinity of the adenosine 3', 5'-diphosphate moiety.

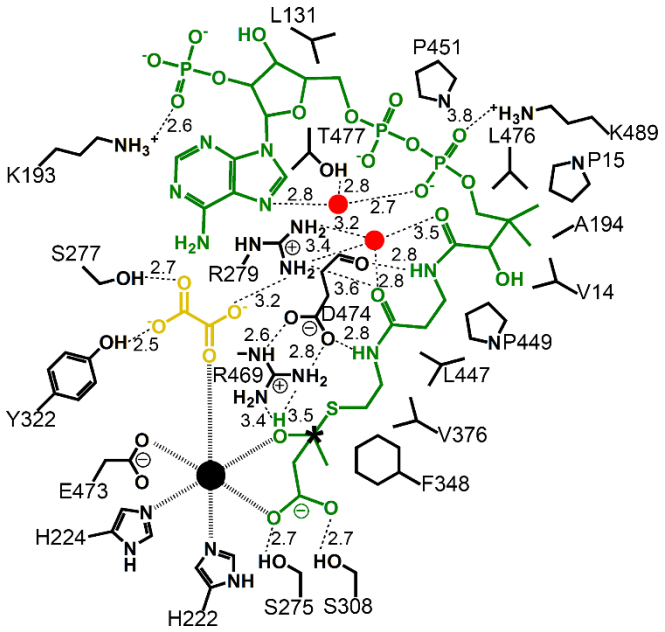
L131
P451
K193
T477
L476
K489
P15
A194
S277
R279
V14
D474
P449
L447
Y322
R469
V376
F348
E473
H224
H222
S275
S308

Figure 12. The binding of a C4-CoA adduct and oxalate in the active site of ObcA.

(*A*) A magnified view for oxalate (yellow), C4-CoA adduct (green), and Co^{2+} (black sphere) is shown; the asterisk indicates the carbon atom in a tetrahedral configuration. In the left panel, the final model is overlaid with an *Fo–Fc* map (2.3 σ), showing the possible connection between the oxalate region and the C4-CoA adduct. However, after refinement, the density between the adduct and oxalate is clearly distinguished, which is shown in the right panel with a *2Fo–Fc* map (1.7 σ). (*B*) Two different orientations with an *Fo–Fc* map (2.3 σ) are shown to indicate that the carbon atom joined to the sulfhydryl group of the adduct is in a tetrahedral configuration. (*C*) A magnified view is displayed for the relative positioning of the ligands, including oxaloacetate (yellow), as well as oxalate and the C4-CoA adduct, both in green. The relative positions were determined by superposing the two complexes. The C3 of oxaloacetate is ~2.6 Å away from the tetrahedral carbon in the C4-CoA adduct, implying that the enolate form of oxaloacetate undergoes a direct nucleophilic attack on the thioester carbonyl carbon of acetyl-CoA.

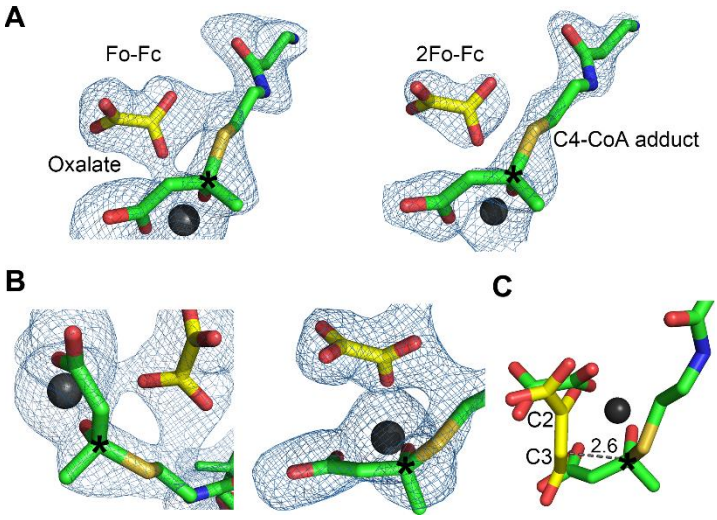
A
Fo-Fc
Oxalate
2Fo-Fc
C4-CoA adduct
B
C
C2
C3
2.6

Figure 13. Activity assay of ObcA.

(*A*) Total oxalic acid production was measured using an oxalate kit (Trinity Biotech). The presence of either Obc1* or ObcA failed to generate oxalic acid, while production of oxalic acid occurred slowly and spontaneously in solution with ObcA, only after continuing the reaction for a long time period (hours to days). Note that diffraction data was collected from ObcA crystals which were incubated at least two weeks. (*B*) The reaction profile is displayed for CoA production as a function of time. The decrease in absorbance at 600 nm resulted from 2, 6-dichlorophenolindophenol, a dye reacting with the free sulfhydryl group of CoA. Differences in the color code represent reactions in the absence of each component indicated. Initial velocity was determined between 60 and 105 s. (*C*) The metal dependency of ObcA activity was assayed but in the presence of different metal ion.

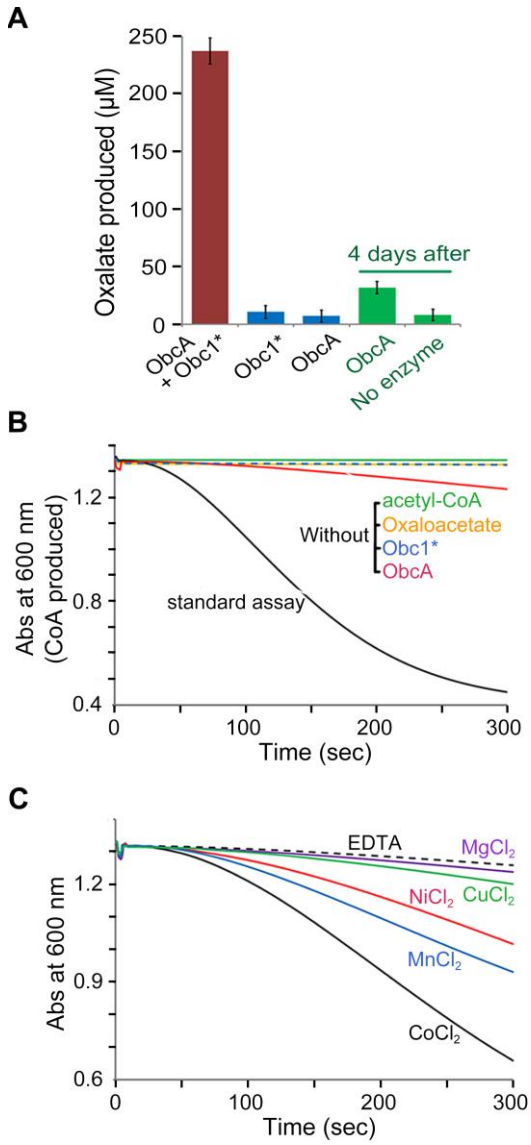
A
Oxalate produced (μM)
250
200
150
100
50
0
4 days after
ObcA + Obc1*
Obc1*
ObcA
ObcA
No enzyme
B
Abs at 600 nm (CoA produced)
1.2
0.8
0.4
acetyl-CoA
Without
Oxaloacetate
Obc1*
ObcA
standard assay
0
100
200
300
Time (sec)
C
Abs at 600 nm
1.2
0.9
0.6
EDTA
MgCl2
NiCl2
CuCl2
MnCl2
CoCl2
0
100
200
300
Time (sec)

Functional analysis of ObcA

An enzymatic analysis was performed using the WT and mutant ObcA enzymes. In particular, production of a free CoA and oxalic acid was measured in a coupled reaction with Obc1*. In the presence of the WT ObcA, Obc1*, and the Co^{2+} ion, the reaction completed in my assay produced oxalic acid as well as CoA (Fig. 13, A-C). The Obc1* enzyme essentially lacks in its own ObcA activity, but not ObcB function, due to mutations at three residues located within the ObcA-like N-terminal domain. Those mutations are H227A, Y326A, and E350A, which correspond to His224, Tyr322, and Glu346, respectively, of *B. glumae* ObcA (Fig. 3) and are essential for ObcA function (see below). Measurement of the total oxalic acid produced, as well as kinetic analysis of CoA production by Obc1*, indicated that Obc1* exhibits less than 0.5% of the WT ObcA activity (Figs. 14 and 15A, and Table 3), with 176- and 328-fold decreases in the k_{cat} value for acetyl-CoA and oxaloacetate, respectively, relative to that of the WT ObcA (Fig. 15B).

A steady-state kinetic analysis for the production of free CoA and measurement of total oxalic acid production indicated that residues interacting with the metal ion as well as oxaloacetate or a bisubstrate adduct play an essential role in enzyme activity (Fig. 14). Greater activity for total oxalic acid production than CoA production is possibly attributable to the experimental condition of oxalic acid production in which the measurement was performed after 5 min of reaction time for each mutant ObcA. Mutations on metal binding residues (Fig. 7A), H222A, H224A and E473A significantly reduced ObcA functions; H224A became essentially inactive, although H222A and E473A has some marginal activity, suggesting that His224 is most important in metal

binding. Similar results were also observed for oxaloacetate-binding residues (Fig. 8A); mutants, such as S275A, S277A, S308A, R279K and R279A also largely defect ObcA activity, except for R279K. Unlike R279A which exhibits less than 5% of the WT ObcA activity, the R279K mutant maintained a nearly identical k_{cat} value with the WT ObcA, but with a 35-fold increase in its K_M for oxaloacetate and only a 3-fold increase for acetyl-CoA (Fig. 8B and Table 3), indicating that the positive charge on Arg279 is crucial for the binding of oxaloacetate. Other mutations also largely affected the K_M value for oxaloacetate, consistent with their proposed structural roles. For example, S277A and S308A exhibited 8- and 27-fold increases, respectively, in the K_M value for oxaloacetate, but with much smaller changes (1- to 2-fold) in the K_M values for acetyl-CoA.

In additions to residues in the metal-coordination shell and oxaloacetate-binding environment, several residues in the acetyl-CoA-binding pocket (Fig. 9) such as Glu346, Leu447, Arg469, and Asp474 were also characterized as essential elements for activity (Fig. 14). Mutations on these residues caused their activities less than 3% of the WT ObcA, consistent with their proposed roles in the binding of acetyl-CoA or adduct. For example, Leu447 is within distance of the CoA moiety to mediate hydrophobic interactions, and Arg469 was suggested in this study to protonate the oxygen atom on the tetrahedral carbon of the adduct, resulting in the hydroxyl group (Fig. 11). Asp474 interacting with Arg469 appears to play a role in positioning of the Arg469 side chain toward the adduct and regenerating Arg469 in a catalytically competent form (see legend of Fig. 16).

While most residues described above play a role in the binding of

substrate or a possible adduct, I conclude that Tyr322 is a key catalytic residue in ObcA reaction, based on its regiospecific location to the C3 atom of oxaloacetate (Fig. 8A; see Discussion). Mutation of Tyr322 with either alanine or phenylalanine also greatly diminished the enzyme activity (4~10% of the WT ObcA activity), suggesting a possible catalytic role of the side chain hydroxyl group in the reaction. In particular, further kinetic analysis of Y322F indicated that catalytic efficiency (k_{cat}/K_M) of the mutant is only 0.3~2.0% of the WT ObcA.

Figure 14. Relative activity assay of ObcA.

The CoA (blue) and total oxalic acid (red) production were measured using the WT and mutant ObcAs. For the relative activity of the CoA production, the initial velocity was determined as shown in Fig. 13B, and those values were compared to that of the WT ObcA. Total oxalic acid produced was measured after 5 min of reaction time. In both assays, measurements were performed with 400 μM acetyl-CoA, 1 mM oxaloacetate, 100 μM $CoCl_2$, 50 nM WT or mutant ObcA, and 800 nM Obc1*, and carried out in triplicate for each sample; error bars correspond to the SEs.

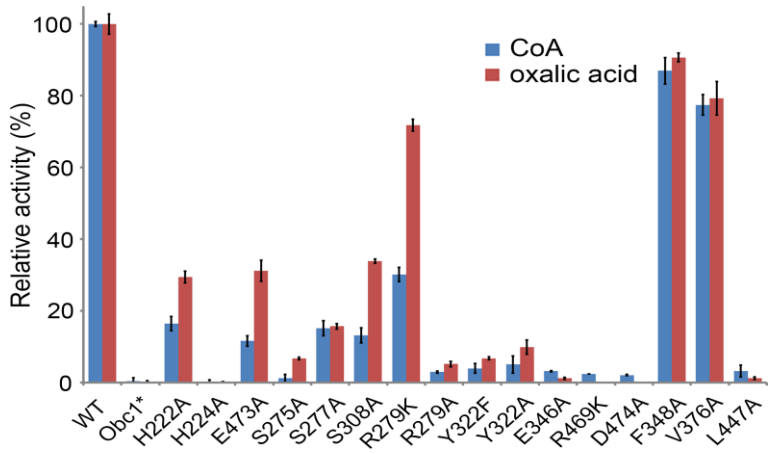
Relative activity (%)
100
80
60
40
20
0
CoA
oxalic acid
WT
Obc1*
H222A
H224A
E473A
S275A
S277A
S308A
R279K
R279A
Y322F
Y322A
E346A
R469K
D474A
F348A
V376A
L447A

Figure 15. Functional features of ObcA and Obc1*.

(*A*) A steady-state kinetic analysis of Obc1* for the production of CoA was performed. The K_M and V_{max} values were obtained using SigmaPlot, with SEs noted in parenthesis. (*B*) A steady-state kinetic analysis of the WT ObcA was performed. The initial velocity was corrected by subtracting the value of Obc1* from that of ObcA, and the K_M and V_{max} values were obtained using SigmaPlot, with SEs noted in parentheses.

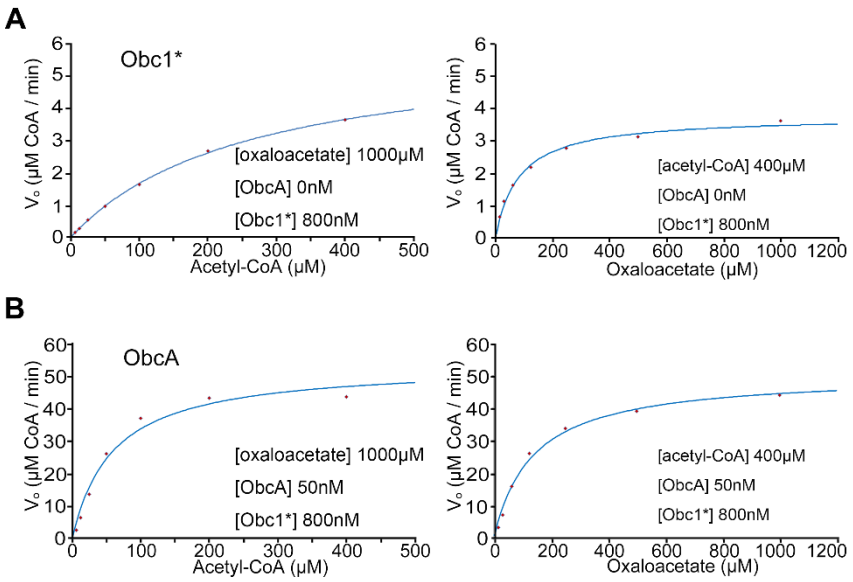
A
Obc1*
V₀ (µM CoA / min)
[oxaloacetate] 1000µM
[ObcA] 0nM
[Obc1*] 800nM
Acetyl-CoA (µM)
[acetyl-CoA] 400µM
[ObcA] 0nM
[Obc1*] 800nM
Oxaloacetate (µM)
B
ObcA
V₀ (µM CoA / min)
[oxaloacetate] 1000µM
[ObcA] 50nM
[Obc1*] 800nM
Acetyl-CoA (µM)
[acetyl-CoA] 400µM
[ObcA] 50nM
[Obc1*] 800nM
Oxaloacetate (µM)

Table 3. Kinetic parameters of ObcA, ObcA mutants, and Obc1*.

		K_M (μM)	k_{cat} (sec^{-1})
WT	acetyl-CoA	58.6 (12.8)	17.6 (1.27)
	oxaloacetate	135.5 (17.3)	16.4 (0.68)
Obc1*		260 (10.4)	0.05 ($2.1*10^{-3}$)
		81.4 (7.48)	0.10 ($1.5*10^{-3}$)
R279K		190 (8.1)	17.0 (0.277)
		4627 (683)	17.2 (1.19)
S277A		52.5 (7.2)	3.45 (0.128)
		1073 (355)	2.88 (0.292)
S308A		155 (8.0)	6.20 (0.114)
		3535 (382)	6.09 (0.283)
Y322F		250 (60.4)	1.54 (0.154)
		4203 (1206)	1.53 (0.200)

The values for K_M and k_{cat} obtained by CoA production are listed for the WT ObcA and four mutant enzymes with marginal activity, with SEs in parenthesis.

Figure 16. The proposed mechanism for ObcA.

Upon the binding of oxaloacetate, the side chain hydroxyl group of Tyr322 could be deprotonated by the C1 carboxylate of oxaloacetate, which is within 3.0 Å. The resulting anionic form of Tyr322 likely serves as a general base and abstracts a proton from the C3 carbon of oxaloacetate in a regiospecific manner, producing an enolate anion intermediate of oxaloacetate. The anion intermediate can be stabilized via interactions with a metal ion bound to the active site, followed by a direct nucleophilic attack on the thioester carbonyl carbon of acetyl-CoA to yield a tetrahedral C6-CoA adduct as a product. In an immediate vicinity of the oxygen atom on a tetrahedral carbon, Arg469 possibly protonates the oxygen atom. The hydrogen bond network from Arg469 to the water molecule via Asp474 could regenerate Arg469; in particular, Asp474 is a solvent-exposed residue, and the nearby water molecule is located in the binding pocket for acetyl-CoA. Note that mutation of either Tyr322, Arg469, or Asp474 greatly affects the enzyme activity (Fig.14).

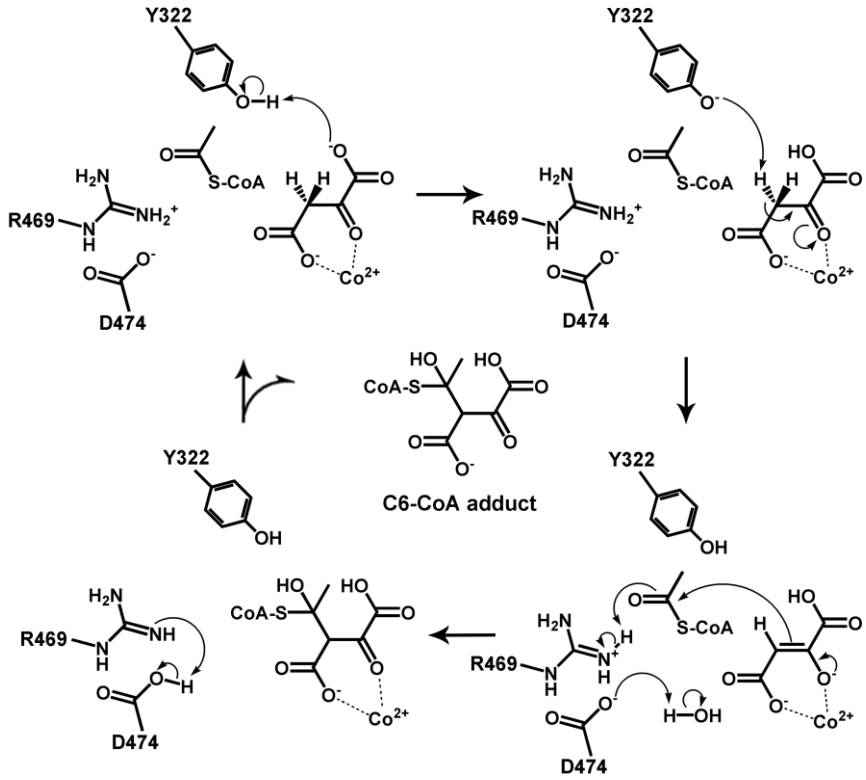
Y322
S-CoA
R469
D474
Co2+
C6-CoA adduct
CoA-S
HO
OH
H2N
NH2+
NH
H-OH

Discussion

In *Burkholderia*, endogenous oxalogenesis occurs using oxaloacetate and acetyl-CoA, the substrates also utilized by citrate synthase in the TCA cycle. However, ObcA and citrate synthase are structurally unrelated (Wiegand and Remington, 1986). Accordingly, apparent functional discrepancies between the two enzymes originate from the distinct architecture of the active site. In citrate synthesis, acetyl-CoA acts as a nucleophile, in which the general base aspartate produces an enolate from acetyl-CoA followed by its direct attack on the C2 carbonyl carbon of oxaloacetate. The intermediate is then hydrolyzed into citrate and CoA (Wiegand and Remington, 1986). In contrast, my structural and functional analyses, together with a previous isotope labeling experiment (Li et al., 1999), suggest that oxaloacetate is a nucleophile for ObcA. Fig. 16 presents a proposed reaction mechanism of ObcA. Specifically, an ObcA-dependent reaction requires formation of an enolate anion intermediate of oxaloacetate, which then attacks the thioester carbonyl carbon of acetyl-CoA to yield a tetrahedral C6-CoA adduct as a product (Li et al., 1999). In particular, Tyr322, which is also conserved in other ObcA homologs (Fig. 3), appears to act as a general base to form an enolate intermediate of oxaloacetate by regioselectively deprotonating the C3 methylene in oxaloacetate (Fig. 8). The resulting enolate anion is likely stabilized by coordinating with the bound metal ion. Consistent with this proposal, mutation of Tyr322 greatly diminished the enzyme activity (Fig. 14 and Table 3). Comparison of the binding mode of oxaloacetate and the bisubstrate adduct in this study indicated that the C3 atom of oxaloacetate is within 2.6 Å from the tetrahedral carbon of the adduct (Fig. 12C), suggesting

that a direct nucleophilic attack of the proposed enolate of oxaloacetate occurs on the *si*-face of the thioester linkage of acetyl-CoA, the trigonal plane facing toward a bound oxaloacetate. Mechanistically, the formation of an enolate intermediate is similar with members of the enolase superfamily, in which a general base abstracts the α-proton of the carboxylate substrate and a metal ion stabilizes the enolate anion intermediate (Gerlt et al., 2005).

Apparently, the proposed ObcA-dependent catalysis (Fig. 16) shares some characteristics with other acetyltransferases involved in the acetylation of histone lysine, carnitine, chloramphenicol, and choline (Dyda et al., 2000, Govindasamy et al., 2004, Jogl and Tong, 2003, Murray and Shaw, 1997, Yuan and Marmorstein, 2013). These acetyltransferases using acetyl-CoA as an acetyl donor commonly produce an acetylated substrate via a proposed tetrahedral intermediate, particularly by employing a general base to deprotonate a substrate, either directly or indirectly via a water-mediated proton wire, and its subsequent attack on the thioester carbonyl carbon of acetyl-CoA. These enzymes containing general acid(s) but lacking metal ions facilitate collapse of the resulting tetrahedral CoA intermediate into an acetylated substrate and CoA. In contrast, the tetrahedral CoA adduct in ObcA is likely stabilized by the bound metal ion and furthermore by the absence of possible general acid(s). Therefore, ObcA exhibits combined features from the enolase and acetyltransferase superfamily, but the presence of the metal-coordination shell and absence of general acid(s) appear to be the key factors for functional diversity. The metal-ligating shell has multiple roles in ObcA-dependent catalysis, not only dictating the binding mode of oxaloacetate to facilitate formation and stabilization of the enolate anion intermediate of oxaloacetate,

but also contributing to the polarization and positioning of the thioester group of the incoming acetyl-CoA for a nucleophilic attack. Furthermore, the metal-coordinating shell also serves as a platform for a direct nucleophilic attack, as well as stabilization of the resulting tetrahedral CoA adduct.

In conclusion, I demonstrated that in the *Burkholderia* species, ObcA utilizes two substrates, oxaloacetate and acetyl-CoA, for the TCA cycle and forms a tetrahedral C6-CoA adduct in an unprecedented manner compared to other acetyl-CoA-dependent reactions. The C6-CoA adduct serves as a substrate for ObcB to produce oxalic acid, acetoacetate, and CoA. Current genome data indicate that ObcA homologs are predominantly present in *Burkholderia* species (Nakata, 2011). My results provide a structural basis for understanding the first step in oxalogenesis using metabolites from the primary metabolic pathway, as well as an example of the functional diversity of an enzyme for survival and adaptation in the growth environment.

Chapter III.

Structural and Functional Analysis of Obc1

Materials and Methods

Cloning and purification of WT Obc1 and its mutants

The gene for Obc1 from *B. thailandensis* (Goo et al., 2012, Nakata, 2011) was amplified by colony PCR and cloned into a modified pET28b expression vector (Merck) containing a TEV protease recognition sequence between the His_5-tag and multiple cloning site. The resulting plasmid containing N-terminal His-tagged Obc1 was transformed into *Escherichia coli* BL21 (DE3) cells (Novagen). After induction of protein expression with 0.5 mM IPTG, *E. coli* cells were cultured for an additional 14–16 h at 20°C. Cells were sonicated in Buffer A containing 50 mM HEPES (pH 7.0), 300 mM NaCl, and 5% (v/v) glycerol. N-terminal His-tagged Obc1 was purified using a HisTrap HP column (GE Healthcare) and eluted with Buffer A plus 250 mM imidazole. The His-tag was subsequently cleaved by treatment with 2 mM dithiothreitol and TEV protease overnight at 22°C using a 20:1 molar ratio of Obc1 to TEV protease. The resulting tag-free Obc1 protein was further purified using a HisTrap HP column and subjected to size-exclusion chromatography using Superdex-200 (GE Healthcare) with Buffer A. The protein concentration was quantified using an extinction coefficient of 129,150 M^{-1} cm^{-1} at 280 nm and calculated using the ProtParam tool in ExPASy (Gasteiger et al., 2003).

For the activity assay, Obc1* was constructed as described in previous chapter (Table 1). Briefly, Obc1* exhibits ObcB activity but essentially lacks ObcA activity due to the introduction of three mutations (H227A, Y326A, E350A) into the active site of the N-terminal domain (Fig. 3). Genes for the various mutants used in the functional assay were amplified by PCR using

Obc1* as a template and mutagenic sequences as primers (Table 4). N-terminal His-tagged Obc1*, Obc1* mutants, and WT ObcA were purified using a HisTrap HP column and then desalted using a HiPrep 26/10 column (GE Healthcare).

Table 4. Primers for Obc1 mutants.

Primers for Obc1 mutagenesis	
R601A_F	ACGGCCGCG**GCC**AGCTTCGGCATCACGATTC
R601A_R	GAAGCT**GGC**CGCGGCCGTCAGCACGTGCTC
S609A_F	ACGATTCGC**GCG**TTCGTCGAAGAGCTCGACC
S609A_R	GACGAA**CGC**GCGAATCGTGATGCCGAAGCTG
F610A_F	ATTCGCTCG**GCC**GTCGAAGAGCTCGACCGCTA
F610A_R	TTCGAC**GGC**CGAGCGAATCGTGATGCCGAAGC
Y701A_F	CCATGTCGC**GCT**AACAGTGACTATTCGAATGTAGTC
Y701A_R	GTCACTGTT**AGC**GCGACATGGAATTCCCACCAGATA
T786A_F	CCCTTCT**GCT**CCGACTACCAATTACCCGTTG
T786A_R	GTCGG**AGC**AGAAGGGAGAACGACCCAGTCT
R856K_F	GCATAAT**AAG**TTCGCTCTGAATGCCGATCCGAG
R856K_R	GAGCGAA**CTT**ATTATGCAGCATCGATGCTTCG
R856A_F	GCATAAT**GCT**TTCGCTCTGAATGCCGATCCG
R856A_R	GAGCGAA**AGC**ATTATGCAGCATCGATGCTTCG
H934A	GTTGAAATGCTTCGCA**GCC**AGTTCAGGCATTGCA
S935A	GAAATGCTTCGCACAC**GCT**TCAGGCATTGCAACC
S936A_F	GCACACAGT**GCA**GGCATTGCAACCGCCCAG
S936A_R	GCAATGCC**TGC**ACTGTGTGCGAAGCATTTC
D997N_F	CTTTAAC**AAT**GTCCGTTCGCTCGCCGGCAC
D997N_R	CGGAC**ATT**GTTAAAGGCTGTTACGTCCACC
D997A_F	CTTTAAC**GCT**GTCCGTTCGCTCGCCGGCAC
D997A_R	ACGGACAG**CGT**TAAAGGCTGTTACGTCCACC
R999K_F	CGATGTC**AAG**TCGCTCGCCGGCACCACCTCTC
R999K_R	GCGAGCGA**CTT**GACATCGTTAAAGGCTGTTACG
R999A_F	CGATGTC**GCT**TCGCTCGCCGGCACCACCTC
R999A_R	CGAGCGA**AGC**GACATCGTTAAAGGCTGTTACG
D1061A	GTCTTTTTACTGGAT**GCT**CACGCGCGTTTAGATG
D1067A	ACGCGCGTTTAGAT**GCT**GGCCACAGCATTCG
H1069A	GCGTTTAGATGATGGC**GCC**AGCATTCGCCGTTAC
S1070A	TTAGATGATGGCCAC**GCC**ATTCGCCGTTACCTG
R1073A	GCCACAGCATTCGC**GCT**TACCTGGCAGCGAG

Sequences are described from 5' to 3'. Reverse (R) primers that can be obtained by reverse complement of forward (F) primer are not shown. Boldfaced-underlined sequences indicate mutated sequences.

Crystallization and data collection

Crystallization was conducted at 22°C using the sitting drop vapor diffusion method. Initial crystals were produced in a buffer containing 0.1 M HEPES (pH 7.0), 1 M sodium citrate tribasic, and 10 mg/mL protein. Later, I found that co-crystallization of Obc1 with 5 mM oxaloacetate and 2 mM acetyl-CoA improved crystal shape and diffracting quality (Fig. 17). However, the added substrates were not bound to the active site. Under these conditions, I obtained a crystal for the apo form of Obc1.

I also report the structure of Obc1 in complex with glycerol in its active site. Crystallization conditions for this complex were the same as those used for the apo form, except that a pre-grown crystal was soaked in the crystallization mother liquor plus 5 mM acetyl-CoA and 10 mM oxaloacetate. During protein purification, glycerol was a component of Buffer A; however, for unknown reasons, it was only bound to Obc1 when the crystal was soaked in the mother liquor containing substrates.

X-ray diffraction data were collected at 100 K with a 0.5° oscillation angle on beamline 7A at the Pohang Accelerator Laboratory (Korea). Ethylene glycol (20% v/v) was used as the cryo-protectant during data collection and the collected image files were processed using iMOSFLM (Battye et al., 2011). The space group of Obc1 crystals is $R3_2$, with one monomer in the asymmetric unit (Table 5). In particular, a high-resolution cut-off of each data set was based on a $CC_{1/2}$ statistical value of about 0.5. The $CC_{1/2}$ statistical value is superior to the R_{merge} or signal-to-noise ratio as a statistical guide for deciding the usefulness of data (Diederichs and Karplus, 2013, Evans, 2011, Karplus and Diederichs, 2012). In this study, the $CC_{1/2}$ value-based resolution cut-off indeed

provided a higher-quality electron density map, compared to the map calculated using data based on the R_{merge} value or signal-to-noise ratio.

Figure 17. Optimized Obc1 crystals.

Crystals were obtained under a co-crystallization with 5 mM oxaloacetate and 2 mM acetyl-CoA. Co-crystallization with substrates significantly improved crystal size and diffraction quality.

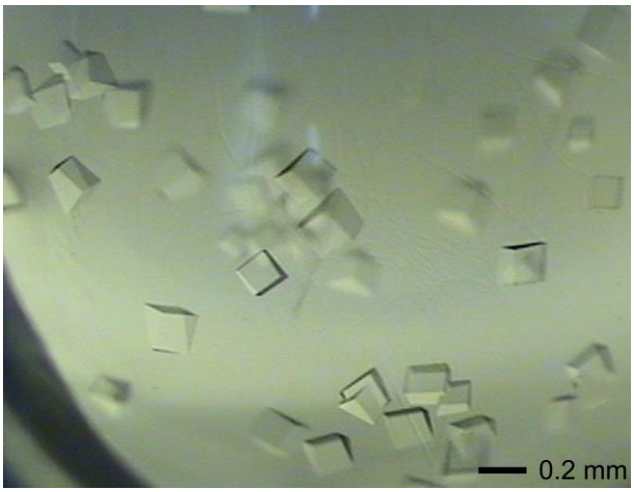
0.2 mm

Table 5. Obc1 data collection and refinement statistics.

Data set PDB ID	**Apo** 5IKY	**Glycerol-bound** 5IKZ
Wavelength (Å)	0.9793	0.9793
Resolution range (Å)	38.8-2.5 (2.6-2.5)[a]	46.35-2.8 (2.9-2.8)
Unique reflections	88989 (8845)	63294 (6257)
Multiplicity	2.0 (2.0)	2.0 (2.0)
Completeness (%)	99.7 (100.0)	100.0 (100.0)
Mean I/sigma(I)	10.4 (1.4)	12.7 (1.6)
Wilson B-factor ($Å^2$)	57.1	57.0
R-merge	0.040 (0.496)	0.056 (0.492)
$CC_{1/2}$[b]	0.998 (0.530)	0.997 (0.461)
CC*[c]	0.999 (0.832)	0.999 (0.794)
Space group	R 3 2 :H	
Unit cell a=b, c (Å)	230.8, 253.7	230.0, 253.8
α=β, γ (°)	90, 120	
Refinement		
R-work[d]	0.198 (0.306)	0.199 (0.300)
R-free[e]	0.227 (0.331)	0.227 (0.332)
No. of atoms		
protein	7835	7848
ligand	1	7
waters	200	207
Protein residues	1048	1047
RMS(bonds) (Å)	0.003	0.003
RMS(angles) (°)	0.72	0.69
Ramachandran favored (%)	96	96
Ramachandran outliers (%)	0.6	0.4
Average B-factor ($Å^2$)	77.9	69.5
protein	78.2	69.9
ligand	54.4	79.7
waters	67.7	54.8

[a]Numbers in parentheses refer to data in the highest resolution shell.

[b]The $CC_{1/2}$ is the Pearson correlation coefficient (CC) calculated from each subset containing a random half of the measurements of unique reflection.

[c]$CC^* = [2CC_{1/2} / (1 + CC_{1/2})]^{(1/2)}$, a statistical guide for deciding useful data, as defined by Karplus and Diederichs (Karplus and Diederichs, 2012).

[d]$R_{work} = \Sigma \, ||F_{obs}|-|F_{cal}|| / \Sigma |F_{obs}|$

[e]R_{free} is the same as R_{obs} for a selected subset (2.25% in Apo form, 5% in Glycerol-bound form) of the reflections that was not included in prior refinement calculations.

Structure determination and refinement

The structure of apo-Obc1 was determined using the molecular replacement program MrBUMP (Keegan and Winn, 2007, Winn et al., 2011) with an apo-ObcA structure (Protein Data Bank code 4NNA) using the N-terminal region of Obc1 as a search model. Unlike the N-terminal region, the quality of the electron density map for the remaining C-terminal region was relatively poor. The initial model was manually built and refined using the programs COOT (Emsley et al., 2010), Buccaneer (Cowtan, 2006, Winn et al., 2011), and PHENIX (Adams et al., 2010). Several cycles of model building and refinement improved the quality of the map, in particular for the C-terminal region. In the final model, 1048 residues were located, except for some highly disordered residues (Table 5). As seen in the structure of ObcA (Fig. 7C), an electron density map for a metal ion was found in the active site of the apo-Obc1 N-terminal domain, even though no metal ion was added during purification or crystallization. Subsequently, the refined structure of apo-Obc1 was used as a starting model for refining Obc1 in complex with glycerol. In particular, an electron density map corresponding to glycerol was identified in the putative active site of the Obc1 C-domain. Further refinement was carried out using PHENIX.

Steady-state kinetic assay

Obc1 enzymatic activity was measured in a manner similar to that for ObcA. In brief, two different assays were employed, each measuring the production of different products. First, a steady-state kinetic assay was performed in the presence of DCPIP, which is reduced by the free sulfhydryl group of CoA, causing a linear decrease in absorbance at 600 nm (Jones and Hirst, 2013, Nakamura et al., 2008, Raychaudhuri et al., 2005). Second, total oxalic acid production was measured using an oxalate assay kit (Trinity Biotech), following the manufacturer's protocol. In both assays, the reaction mixture contained Co^{2+} ion as the most effective ion for ObcA activity (Fig 13C).

Using DCPIP, a steady-state kinetic assay was performed at 30°C in a reaction mixture containing 50 mM HEPES (pH 8.0), 100 mM NaCl, 120 μM DCPIP, 100 μM $CoCl_2$, and 7.8–500 μM acetyl-CoA and oxaloacetate. Then 250 nM ObcA was added to the reaction mixture and pre-incubated for 10 min at 30°C to produce C6-CoA adducts that served as substrates for the Obc1 C-terminal domain. After pre-incubation, 100–2000 nM Obc1* or its mutant was added to the reaction mixture for adduct cleavage to free CoA, acetoacetate, and oxalic acid. A decrease in absorbance at 600 nm was measured using a UV-Vis spectrophotometer (Jasco) and the initial velocity was determined from 70 to 130 s. The initial velocity was used to determine the CoA production per minute based on a standard reaction curve. K_m and V_{max} values were obtained by fitting initial velocity versus substrate concentration data to the Michaelis–Menten equation using SigmaPlot. In this analysis, I assumed that the concentration of the C6-CoA adduct produced was equal to the concentration of the substrates acetyl-CoA and oxaloacetate. Unlike the kinetic assays, to

determine the relative activity of the Obc1* mutants, the assays were performed using 500 μM substrate and 100 nM Obc1* or its mutants, and the initial velocity was determined.

Total oxalic acid production was measured at 30°C using the reaction mixture for kinetic analysis in the presence of 500 μM acetyl-CoA and 500 μM oxaloacetate but without DCPIP. In brief, 500 nM ObcA was added to the reaction mixture and incubated for 5 min. Cleavage of the C6-CoA adduct was initiated and incubated for another 5 min after the addition of 100 nM Obc1*. The resulting reaction mixture was mixed with an oxalate assay reagent and the absorbance at 590 nm was measured after 5 min. The concentration of oxalic acid was calculated from a standard curve.

Results

Overall structure of apo Obc1

The bifunctional enzyme Obc1 has two structurally and functionally distinct domains (Fig. 2A): an N-domain consisting of an ObcA-like N-terminal region (residues Val2 to Ser528) and a C-domain consisting of an ObcB activity-exhibiting C-terminal region (residues Arg529 to Gln1106). These two domains are arranged in an elongated manner (i.e., 110 Å long and 56 Å wide); therefore, there are no extensive interactions between the two domains. The active sites of the two domains are separated by 47 Å and oriented in an opposite direction (Fig. 18).

Monomeric Obc1 was identified in an asymmetric unit and no obvious oligomeric structure was identified by crystallographic symmetry, consistent with chromatographic analysis that Obc1 is monomeric. The N-domain of Obc1 exhibits 52% sequence identity with ObcA (Fig. 19) and therefore its structure is essentially identical to that of ObcA (PDB code 4NNA-C). Specifically, the $(\beta/\alpha)_8$-barrel fold of the Obc1 N-domain is superimposable with ObcA (Fig. 20), within a root-mean square deviation of 1.0 Å for 482 Cα atoms and a Z-score of 51.2 using the structure-similarity search program DALI (Holm and Rosenstrom, 2010). Structural analysis revealed the presence of a metal-binding site and the relative locations of residues in the active site. Given that detailed structural and functional features of ObcA have been reported, I decided to focus on C-domain features.

Figure 18. The overall structure of Obc1.

The overall structure of Obc1 in apo form is shown with its N-domain (green). The C-domain consists of two regions: a cap domain (cyan) and an α/β hydrolase fold (magenta). For clarity, β-strands are indicated in blue, except β1 (red) in the N-domain. The proposed active sites of the C-domain are located in a crevice between the cap domain and the α/β hydrolase fold, and the position of the catalytic Ser935 residue near helix α30 is marked with an asterisk in black. In this orientation, the active site of the C-domain is directed out of the page, directly toward readers, but an opening to the active site of the N-domain is oriented by 180° relative to the C-domain. The active site of the N-domain is indicated with a metal ion in a black sphere.

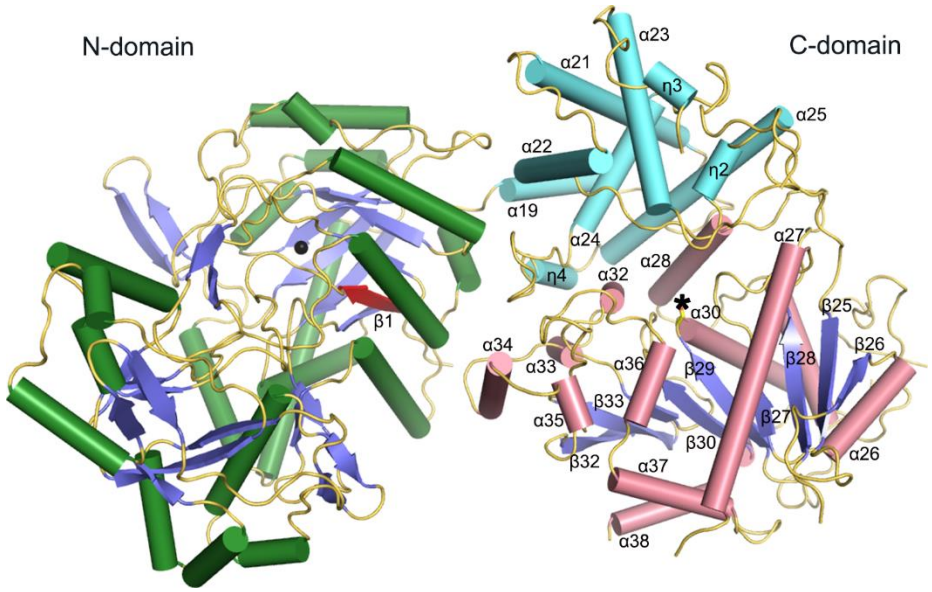
N-domain
C-domain
α23
α21
η3
α25
α22
η2
α19
α24
α27
α28
η4
α32
α30
β25
α34
α33
α36
β29
β26
β28
β33
α35
β27
β30
α26
β32
α37
α38
β1

Figure 19. Sequence alignment of Obc1 with its homologs.

The amino acid sequence of Obc1 from *B. thailandensis* (WP_009896555.1) is compared with that of other homologs, including those from *B. mallei* (WP_004188532.1), *B. pseudomallei* (YP_111366.1), *B. andropogonis* (WP_046153766.1), *B. glumae* (WP_015877888.1), and *B. cepacia* (WP_048244856.1). Note that unlike the other homologs, *B. glumae* and *B. cepacia* (red diamonds) require two enzymes for oxalogenesis, but only ObcA, and not ObcB, shows sequence homology with the Obc1 N-domain. Highly conserved residues are shown in red and boxed in blue, while strictly conserved residues are shown with a red background. Secondary structural elements defined in the Apo form of Obc1 are shown for the corresponding Obc1 sequences. Selected residues are indicated with different notations, including the metal-coordinating residues and catalytic residue of the N-domain (His225, His227, Tyr326 and Glu350; *green triangle*), catalytic triad (Ser935, Asp997 and His1069; *blue inverted triangle*), and putative oxyanion hole-forming residues (Arg856 and Arg999; *green circle*). In particular, His934, a proposed catalytic residue for lyase activity, is marked with a *gray star*. This figure was prepared using ESPript (Robert and Gouet, 2014).

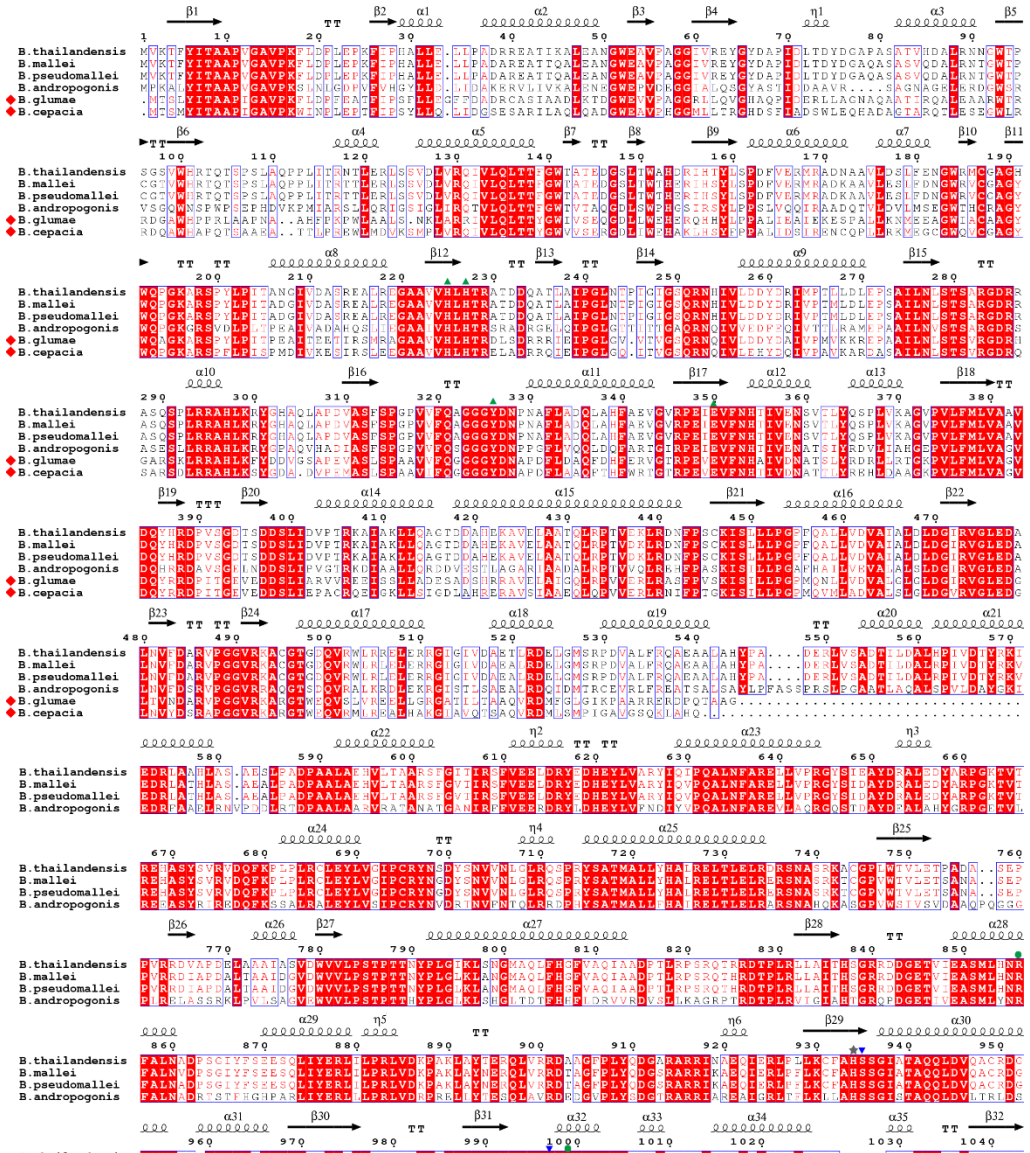
B.thailandensis
B.mallei
B.pseudomallei
B.andropogonis
B.glumae
B.cepacia

Figure 20. The N-terminal domain of Obc1.

The N-domain is shown in a different orientation from that of Fig. 18. The $(\beta/\alpha)_8$-barrel fold is within a circle.

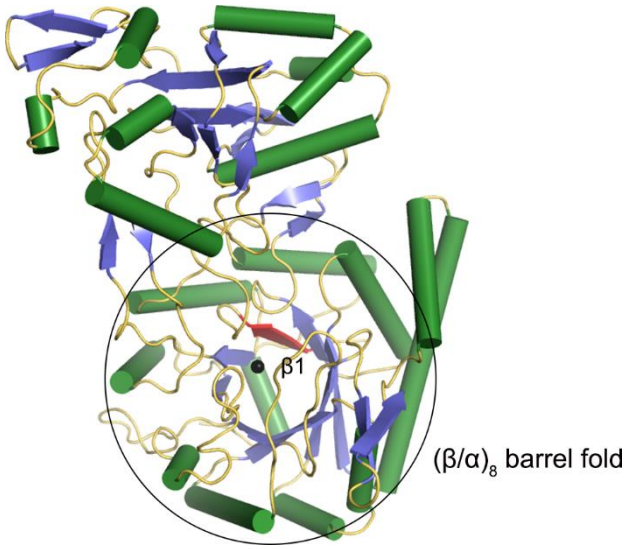
β1
(β/α)8 barrel fold

C-domain of apo Obc1

The Obc1 C-domain (residues Arg529 to Gln1106) extends from the bottom of the N-domain $(\beta/\alpha)_8$-barrel fold and forms an independent domain that does not interact extensively with the N-domain. The core structural region adopts an α/β hydrolase fold, in which the central β-sheet is packed with flanking α-helices on both sides (Fig. 18). The C-domain has structural features common to canonical α/β hydrolases (Kourist et al., 2010). From the topological view, the C-domain consists of two structural subdomains (Fig. 18). The first region includes Ser740 to Gln1106 and forms an α/β hydrolase fold (Fig. 21). The second subdomain (Arg529 to Ala739) is located over a concave region formed by an α/β hydrolase fold, resulting in a crevice between the two regions. Residues Arg529 to Ala739 (hereafter, I will call this region the cap domain) predominantly form an α-helical fold, with two layers of anti-parallel helices. Specifically, just after the N-domain, two long adjacent α-helices α19 and α20/21 are oriented in an anti-parallel fashion and form a surface layer of cap domain. Underneath this surface layer, other anti-parallel helices α24 and α25 are located in a perpendicular orientation relative to the surface layer helices. In addition to these elements, helices α22, α23, and η3 form a four-helix bundle-like fold with the C-terminal region of α21. Due to a kink in the middle of the surface layer α-helices, the cap domain exhibits a convex surface and a concave interior. This cap domain is oriented such that a concave region sits on the edge of the β-sheet in the α/β hydrolase fold, resulting in the formation of a crevice on one side of the β-sheet that serves as the active site of the C-domain (see below).

Following the cap domain α25, a long loop connects a β-strand (i.e., β25)

to form an α/β hydrolase fold including Ser740 to Gln1106 (Figs. 19 and 21). In the α/β hydrolase fold, nine β-strands (β26, β25, β28, β27, β29, β30, β31, β33, β32 in order) constitute a central β-sheet, in which β32 is the innermost strand near the N-domain, and β26 is located farther from the N-domain and forms the surface of Obc1. In the middle of the central β-sheet, six strands (β28, β27, β29, β30, β31, and β33) are in a parallel orientation, with each C-terminal end pointing to the concave interior of the cap domain. At the ends, the other three β-strands are in an anti-parallel orientation (Fig. 21). Helices α26, α29, α30, α31 are located on the backside of the β-sheet where the cap domain surface helices α19 and α20/21 are stretched out; this leaves this side of the central β-sheet inaccessible from the solvent. In particular, helix α28 on this side is located under the surface layer of the cap domain. The remaining helices are positioned at the other side of the central β-sheet in an arrangement that generates a crevice on the C-terminal end of the central β-sheet.

Figure 21. Topology diagram of C-terminal of Obc1.

The topology of the α/β hydrolase fold in the Obc1 C-domain is shown. Color codes are the same as those in Fig. 18, and the catalytic triad is indicated. This figure was prepared using TopDraw (Bond, 2003). Given that the Obc1 N-domain is essentially identical to that of ObcA, its topology was not presented.

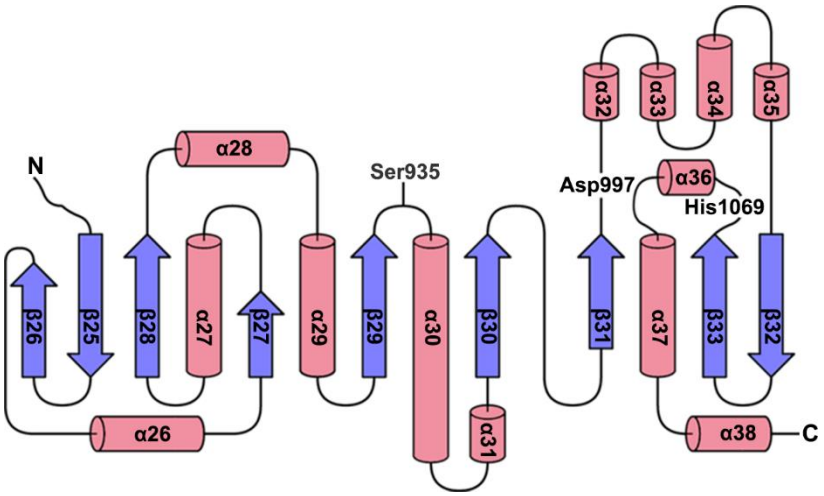
N
α28
Ser935
α32
α33
α34
α35
Asp997
α36
His1069
β26
β25
β28
α27
β27
α29
β29
α30
β30
β31
α37
β33
β32
α26
α31
α38
C

Active site of Obc1 C-domain

The crevice on the Obc1 C-domain suggested the location for putative ObcB activity in the bifunctional enzyme Obc1. Moreover, a DALI-based structure similarity search indicated the presence of a catalytic triad (Ser-His-Asp) in the Obc1 crevice. Specifically, the search revealed that the most similar α/β hydrolase was pancreatic lipase-related protein 2 (PDB code 2PVS) (Eydoux et al., 2008); however, this protein only had a Z-score of 9.3 and 8% sequence identity. Due to low similarity in structure and sequence, these two α/β hydrolases exhibited limited structural conservation in the positions of the central β-strands, with large differences in the location of the flanking α-helices. Despite these differences, structural superposition of the Obc1 C-domain with pancreatic lipase-related protein 2 showed conservation of the catalytic triad (Ser-His-Asp) in both position and relative orientation. In Obc1, the putative catalytic triad consists of Ser935, Asp997, and His1069 located in a loop region between β29 and α30, β31 and α32, and β33 and α36, respectively (Figs. 21 and 22A). Not surprisingly, these residues are clustered in a crevice in the C-domain, and their relative locations are conserved in other α/β hydrolases, consistent with members of this superfamily (Nardini and Dijkstra, 1999).

The Obc1 C-domain displays unique features in its active site, in addition to many structural features conserved in the α/β hydrolase family of proteins (Kourist et al., 2010). First, a GxSxG sequence motif (x; any residue) containing a nucleophilic serine residue was not found; instead, an AH-S_{935}-SG sequence motif was observed in the Obc1 C-domain. Second, an HGGG motif, a tetrapeptide conserved in many α/β hydrolases for an oxyanion hole, was not found. In general, the HGGG motif is located in a part of the loop region that

is near a nucleophilic serine residue. In this motif, the main chain nitrogen atoms from glycine stabilize the binding of a tetrahedral reaction intermediate by forming a hydrogen bond with negatively charged oxygen atoms in the intermediate. In this study, structural superposition indicated that a proposed oxyanion hole conserved in the α/β hydrolase fold corresponded to a loop region including Ser785-Thr786-Pro787 that connects β27 and α27 in the immediate vicinity of Ser935 (Fig. 22A). In other α/β hydrolases, the HGGG motif has been found to be oriented in such a manner that the side chain of histidine points to the inner side of the loop, and the main chain nitrogen atoms of glycine are exposed to nucleophilic serine. However, the side chain hydroxyl group of Thr786 in the Obc1 C-domain protrudes from the corresponding loop and is located 2.5 Å from Ser936, a residue next to nucleophilic Ser935, and 2.5 Å from a water molecule that also forms a hydrogen bond with Ser935, a putative catalytic nucleophile (Fig. 22A). Given this structural feature and the presence of proline at amino acid number 787, the main chain nitrogen atoms in the loop region are unavailable for hydrogen bonding, suggesting that this loop may not serve as an oxyanion hole in Obc1. Instead, positively charged Arg856 and Arg999 are in the vicinity of nucleophilic Ser935. In particular, Arg999 appears to be very dynamic based on its disordered electron density.

Figure 22. The active site of Obc1.

(*A*) The catalytic triad and a putative oxyanion-binding site are shown in the apo structure of Obc1, with the same color codes as in Fig. 18. Possible hydrogen bonds are indicated with a dashed line. A loop of Ser785-Thr786-Pro787 (green) and two arginine residues (Arg856 and Arg999) are presented. A water molecule (red sphere) near Ser935 mediates possible hydrogen bonds to nearby residues. Note that the side chain of Thr786 points outward and its hydroxyl group interacts with the water molecule, and Ser785 and Pro787 are removed for clarity. (*B*) Zoomed-out view of the active site showing the stereoview of Obc1 in glycerol-bound form. Bound glycerol (green) is overlaid with a *Fo-Fc* electron density map contoured at 3.0 σ. Other residues crucial for activity are also indicated. Note that His934 forms a possible hydrogen bond with the hydroxyl group of glycerol. (*C*) Active site interactions in glycerol-bound Obc1. Putative hydrogen bonds (dashed lines) and corresponding interatomic distances (Å) are shown. One exception is the interatomic distance between glycerol (green) C2 and NE2 in His934.

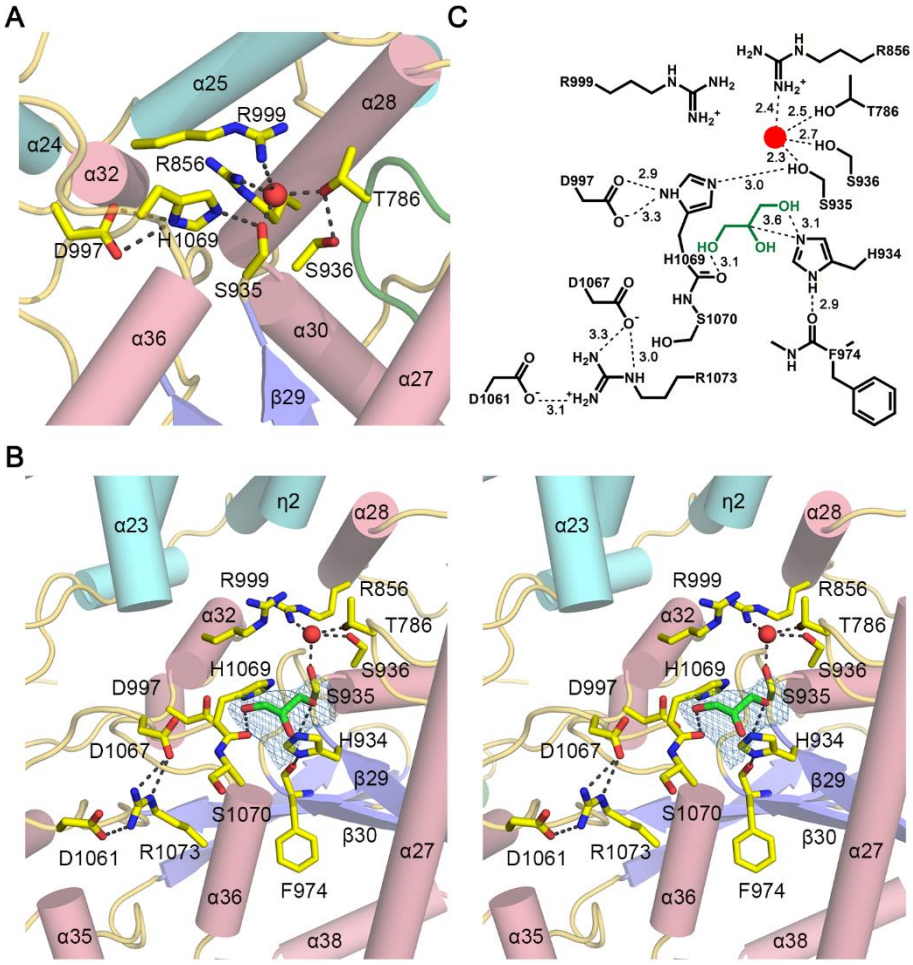
A
α25
α28
R999
α24
α32
R856
T786
D997
H1069
S936
S935
α36
α30
α27
β29
C
R999
R856
T786
S936
S935
D997
H1069
H934
D1067
S1070
F974
D1061
R1073
B
α23
η2
α28
R999
R856
α32
T786
H1069
S936
D997
S935
H934
D1067
β29
S1070
β30
α27
D1061
R1073
α36
F974
α35
α38

The binding of glycerol in the Obc1 C-domain

In my experimental conditions, I was unable to detect the binding of a C6-CoA adduct in the Obc1 C-domain. Instead, I characterized glycerol bound to the Obc1 C-domain. The resulting electron density map suggested that the glycerol-binding site is located at the proposed crevice surrounded by an α/β hydrolase fold and a cap domain (Fig. 22B). Specifically, glycerol was found at the entrance of the crevice, near the catalytic triad. In fact, glycerol is about 3.4–4.0 Å from the side chains of His1069 and Ser935. Based on the current binding environment, it is chemically sensible in glycerol that the C2 carbon and hydroxyl group on *pro-S* C1 is located near the side chain nitrogen of His934, and that the hydroxyl groups at *pro-R* C3 positions are located near the main chain carbonyl oxygen of His1069 (Fig. 22C).

Functional analysis of Obc1

There is no direct structural evidence for the existence of a true substrate-binding site, and functional roles of residues near the proposed active site have been elusive. Therefore, I selected 19 residues in the C-domain for site-directed mutagenesis to explore their functional roles. These residues form the putative catalytic triad (Ser935, Asp997, and His1069), possible oxyanion-binding sites (Ser785, Thr786, Arg856, Ser936, and Arg999), and the putative binding site for a C6-CoA adduct along the crevice and on the surface of the cap domain (Arg601, Ser609, Phe610, Tyr701, His934, Asp1061, Asp1066, Asp1067, Ser1070, Arg1072, and Arg1073).

Two different assays were performed using various Obc1 mutants. Previously, I constructed Obc1* that has three mutations (H227A, Y326A, E350A) in the N-domain to eliminate any possible ObcA activity (Table 3). All Obc1 mutants used for functional analysis in this study were engineered to have a mutation at a designated residue in the C-domain, as well as three mutations in Obc1*. One assay was used to detect the formation of product CoA, and another assay was used to measure oxalic acid production. Preliminary experiments indicated that the maximal initial velocity of Obc1 could be achieved in the presence of ObcA, and under these conditions there were no differences in the initial velocity between WT Obc1 and Obc1* (Fig. 23A, red and black curve). Under my kinetic assay conditions, I also found that a C6-CoA adduct produced from ObcA was stable and could not be converted into CoA in the absence of Obc1 or Obc1* (Fig. 23A), validating that the formation of CoA from the adduct is enzyme-dependent (Fig. 2A).

Among the Obc1 mutants, the activities of three mutants (S785A, D1066A,

R1072A) were essentially identical to that of Obc1*, but other mutants exhibited reduced activities (Fig. 23B). Putative catalytic triad mutants (S935A, D997N, D997A, or H1069A) had significantly impaired enzyme activities, indicating that Ser935, Asp997, and His1069 do indeed form a catalytic triad. Specifically, the production of CoA in these four catalytic triad mutants was approximately 1.8% of Obc1* activity, and oxalic acid production was 5.9–8.3% relative to that of Obc1*. Putative oxyanion-binding site mutants provided interesting results. Compared to Obc1*, T786A and S936A mutants exhibited about 8.5% and 21.0% CoA production, and 12.2% and 34.9% oxalic acid production, respectively. These results suggest that an interaction between Thr786 and Ser936 (Fig. 22A) may be important for maintaining the structural integrity of a Ser785-Thr786-Pro787 loop near catalytic Ser935. Interestingly, two arginine residues, Arg856 and Arg999, were crucial for activity, further supporting my proposal that these two residues could serve as an oxyanion-binding site in Obc1 (Fig. 22A). Specifically, R856A and R999A mutants essentially lost their enzymatic features, but their activities were somewhat restored in R856K and R999K mutants (Fig. 23B). Subsequent steady-state kinetic analyses on R856K and R999K mutants indicated that Arg856 and Arg999 are likely critical catalytic residues, given that these mutants had significant decreases in *kcat* but not *Km* (Fig. 24A and Table 6). Specifically, the *Km* values of the R856K and R999K mutants were 44.2 and 67.1 μM, close to the *Km* of Obc1*; however, their *kcat* values were 3.9% and 15.7% of Obc1*, respectively. Therefore, relative to Obc1*, their catalytic efficiency was 6.0% for R856K and 15.7% for R999K. These results show that a positive charge in these two residues is crucial for catalysis.

Mutations of residues along the crevice or on the surface of the cap domain suggest that residues along the crevice of the α/β hydrolase fold, but not the surface of the cap domain, play an important role in catalysis (Figs. 23B and 24B). Specifically, mutation of Tyr701, Asp1061, Asp1067, Ser1070, or Arg1073 resulted in significant loss of activity despite the fact that these residues are far away from the catalytic Ser935 residue or the glycerol-binding site. In particular, four residues (Asp1061, Asp1067, Ser1070, and Arg1073) are clustered in a loop and a helix between β42 and α36 (Figs. 20 and 24B), indicating that this protruding region can serve as a binding site for a CoA moiety. Cap domain residues including Arg601, Ser609, and Phe610 were relatively tolerant to mutation, indicating that these regions do not participate in catalysis (Figs. 23B and 24B). I further found that His934, a residue adjacent to catalytic Ser935, is crucial for activity (Fig. 22B). An H934A mutant exhibited 5.3% CoA production and 16.8% oxalogenesis relative to Obc1* (Fig. 23B). Further kinetic analysis of H934A indicated that *kcat* was largely affected by mutation, and its value was 7.3% of Obc1*, but no significant change in *Km* was observed (Fig. 24A and Table 6), resulting in a catalytic efficiency of approximately 6.5% of Obc1*. These functional data and the vicinity of His934 to catalytic Ser935 lead me to propose that His934 serves as a catalytic base/acid for cleavage of the C4-S bond in the C6-CoA adduct (Fig. 2A; see Discussion), resulting in the formation of acetoacetate and CoA. Consistent with this, His934 in Obc1 is conserved in other homologs among *Burkholderia* species (Fig. 19).

Figure 23. Obc1 activity assay.

(*A*) Reaction progress curve showing the production of CoA as a function of time. Reaction mixtures containing 500 μM acetyl-CoA and oxaloacetate were identical to those of the kinetic assays, as described in **Materials and Methods**. Measurements were initiated by adding 100 nM WT Obc1 or Obc1*. However, in the five independent assays in the figure, only the enzyme(s) indicated were included in the assay. (*B*) Relative activity of Obc1* and its variants. For Obc1* activity, the initial velocity for CoA production was 72.2 μM/min (blue), as determined in panel (*A*), and the total oxalic acid produced was 347.6 μM for 5-minute reaction (red). These values were compared with the values obtained for each mutant. For both assays, measurements were performed in triplicate (n=3), with 100 nM Obc1* or its mutants, and values are reported as means with SE. Specifically, three independent enzyme purifications were performed. The activities of the mutants, such as S785A, R1066A, R1072A, were identical to that of Obc1*; therefore, these residues were not included in this figure.

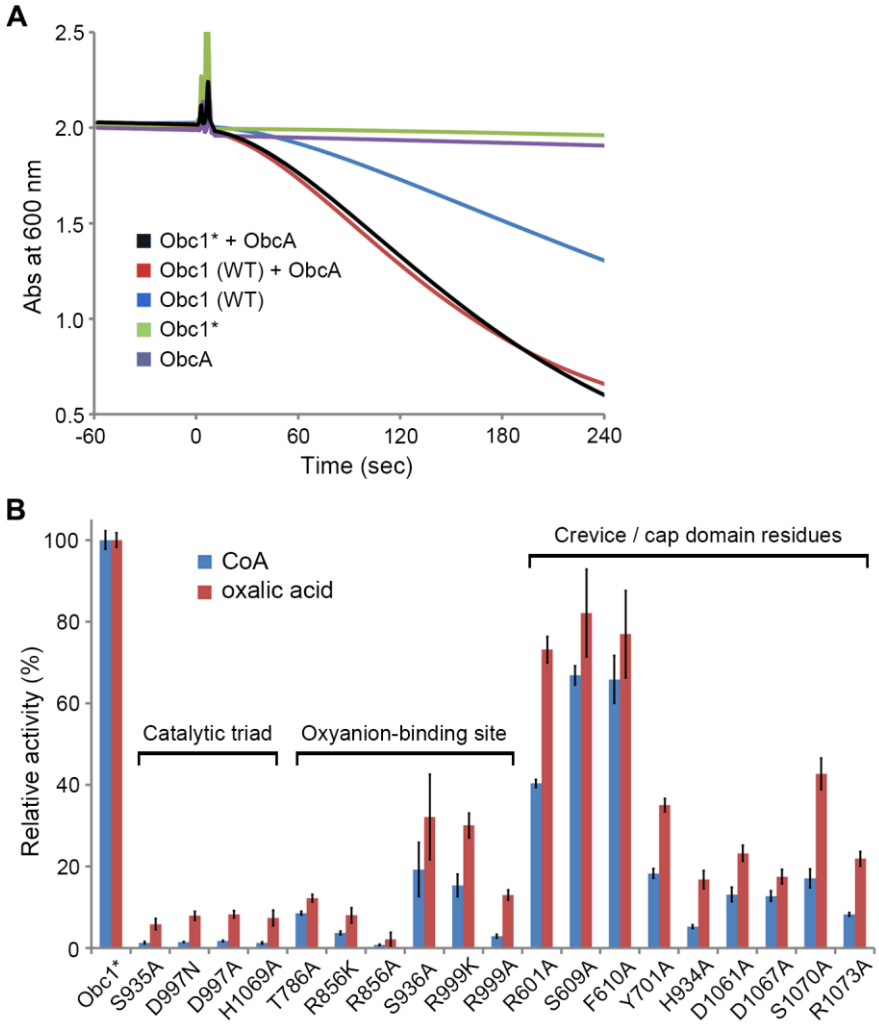
A
Abs at 600 nm
Time (sec)
Obc1* + ObcA
Obc1 (WT) + ObcA
Obc1 (WT)
Obc1*
ObcA
B
Relative activity (%)
CoA
oxalic acid
Catalytic triad
Oxyanion-binding site
Crevice / cap domain residues
Obc1*
S935A
D997N
D997A
H1069A
T786A
R856K
R856A
S936A
R999K
R999A
R601A
S609A
F610A
Y701A
H934A
D1061A
D1067A
S1070A
R1073A

Figure 24. Kinetic analysis and surface representation of Obc1.

(*A*) A steady-state kinetic analysis of CoA production from Obc1* and three mutant enzymes. In this assay, the concentration of the C6-CoA adduct was assumed to be equal to that of acetyl-CoA or oxaloacetate. The regression curve was prepared using SigmaPlot, and the kinetic parameters of the enzymes are indicated in Table 6. (*B*) Surface representation of the Obc1 C-domain. Color codes are as follows: N-domain (green), cap domain (cyan), α/β hydrolase domain (gray), and catalytic Ser935 (red). The surface of residues is indicated in magenta if they significantly affected Obc1 activity. Residues relatively tolerant to mutation are indicated in white. Buried residues, such as Phe610, Thr786, Arg856, Ser936, and Asp997, are not labeled.

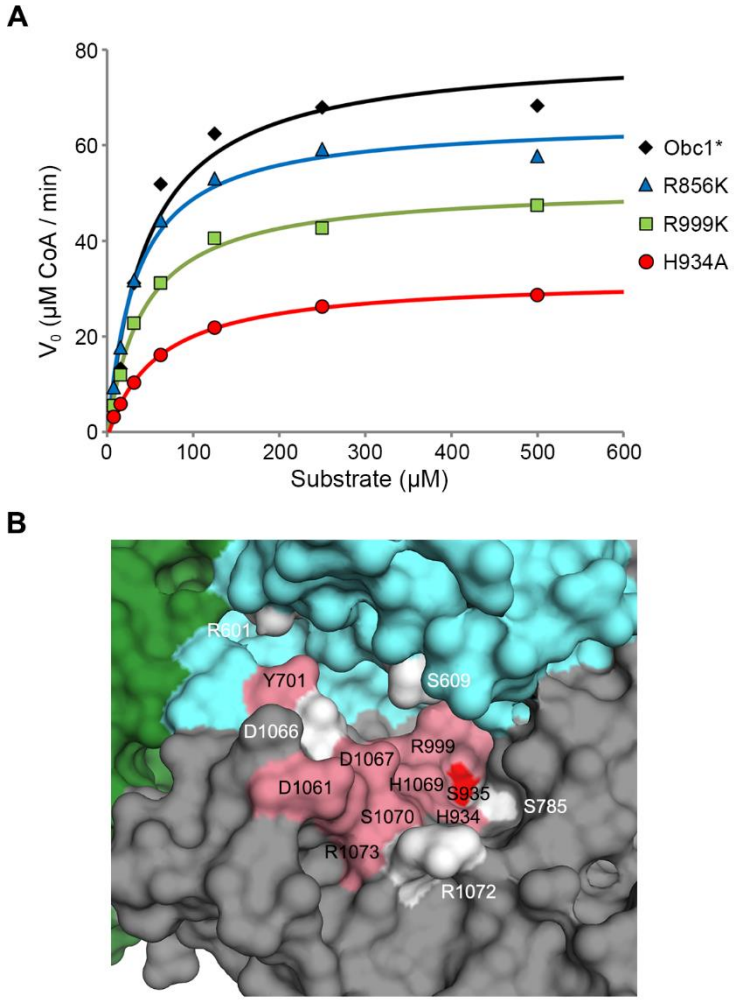
A
80
60
40
20
0
V_0 (µM CoA / min)
0
100
200
300
400
500
600
Substrate (µM)
Obc1*
R856K
R999K
H934A
B
R601
Y701
S609
D1066
R999
D1067
D1061
H1069
S935
S785
S1070
H934
R1073
R1072

Table 6. Kinetic parameters of Obc1* and its mutants.

	kcat (sec^{-1})	*Km* (μM)	*kcat*/*Km* ($sec^{-1}mM^{-1}$)
Obc1*	13.07 (0.17)	67.0 (8.5)	194.9
R856K	0.51 (0.03)	44.2 (3.8)	11.6
R999K	2.05 (0.14)	67.1 (9.7)	30.6
H934A	0.95 (0.10)	74.7 (9.2)	12.7

Numbers in parentheses refer to SE (n=3). Specifically, three independent purifications and measurements of Obc1* or mutant were performed.

Discussion

Structure determination and *in vitro* functional analyses unraveled details about Obc1. Specifically, I found that the Obc1 C-domain exhibits ObcB-like function. It is unusual that functionally identical proteins have a completely different amino acid sequence and number of residues (i.e., approximately 600 residues for the Obc1 C-domain vs. 176 residues for ObcB). In addition, sequence analyses of ObcB using BetaWrap (Bradley et al., 2001) and Phyre2 (Kelley et al., 2015) suggested that ObcB has a β-helix structure, in which parallel β-strands are associated in a helical pattern. Therefore, the Obc1 C-domain and ObcB are dissimilar in all aspects of protein features including sequence, length, and structure. However, a lack of structural information on ObcB precludes further discussion about these unusual discrepancies.

Recent structural studies also revealed another example of a bifunctional enzyme. In *Arabidopsis thaliana* and the parasitic nematode *Haemonchus contortus* (Lee and Jez, 2013, Lee and Jez, 2014), there is a phosphobase methylation pathway. In *A. thaliana,* a bifunctional enzyme with N- and C-terminal domains catalyzes the successive methylation of phosphoethanolamine to form phosphocholine. Interestingly, these reactions are catalyzed by two monofunctional enzymes in *H. contortus*, with each enzyme exhibiting identical catalytic activity to that of a corresponding domain of the *A. thaliana* bifunctional enzyme.

Based on the structural and biochemical data presented here, the following reaction mechanism for Obc1 is proposed (Fig. 25). With high identity both in sequence and structure to ObcA, the Obc1 N-domain should catalyze its first

reaction by following the previously reported mechanism for ObcA (Fig. 16). In the Obc1 N-domain, two different substrates, acetyl-CoA and oxaloacetate, are converted into a C6-CoA adduct (Fig. 2A). Tyr326, a proposed key catalytic base, and other active site residues including metal-coordinating residues are conserved in the Obc1 N-domain (Fig. 19). Given that the C6-CoA adduct from the first reaction is not chemically labile and the liberation of CoA occurs in Obc1*-dependent catalysis (Fig. 23A), the second step should occur in the C-domain and involve the release of three products, namely, oxalic acid, acetoacetate, and CoA. This second enzyme reaction requires cleavage of two different bonds, the C2-C3 bond and the C4-S bond in the C6-CoA adduct (Fig. 2A). From a chemical structure perspective, C2-C3 bond cleavage accounts for oxalic acid production, and C4-S bond cleavage is responsible for the release of acetoacetate and CoA. It is highly evident that within the C-domain crevice, the catalytic triad is responsible for C2-C3 bond cleavage in a manner identical to other serine hydrolases that cleave C-C bonds between trigonal and tetrahedral carbon atoms (Buller and Townsend, 2013, Nardini and Dijkstra, 1999). Specifically, given that C2 in the C6-CoA adduct is the only sp^2-carbon, Ser935, upon activation by His1069, performs nucleophilic attack on the C2 carbonyl carbon, forming a tetrahedral reaction intermediate (Fig. 25, steps I and II). The negative charge on the enolate oxygen atom of the tetrahedral intermediate could be stabilized by the presence of Arg856 or Arg999 (Fig. 23B and Table 6). Subsequent collapse of the tetrahedral intermediate by His1069 as a proton donor cleaves the C2-C3 bond and leaves an acyl moiety covalently attached to Obc1 (Fig. 25, step III). The resulting acyl-Obc1 complex is subsequently hydrolyzed by a water molecule, leading to the release of one

molecule of oxalic acid (Fig. 25, steps IV and V). The two other products, acetoacetate and CoA, should be liberated from the remaining CoA adduct (Fig. 25, steps II and III).

My analyses suggest a catalytic role for His934 in the cleavage reaction of the C4-S bond, leading to the production of acetoacetate and CoA. First, the presence of a hydrogen-bonding network supports that His934 acts as a catalytic base during an initial stage of catalysis and later as a catalytic acid (Fig. 25, steps II and III). Specifically, the ND1 atom (nitrogen near Cα) in the His934 side chain likely forms a hydrogen bond with the main chain carbonyl oxygen of Phe974 (Fig. 22, B and C), allowing the NE2 atom (nitrogen far from Cα) to exist in a deprotonated state for a catalytic base. Furthermore, the binding mode of glycerol could provide a clue to that of a C6 moiety in the C6-CoA adduct (Fig. 25, step I). If I assume that the C6-CoA adduct, whose structure is based on a C4-CoA adduct previously identified (Figs. 9-12), is bound to the active site of the Obc1 C-domain, then the C2 atom of the adduct should be placed toward the catalytic Ser935 residue (Fig. 25, step I). This placement suggests that the *pro-S* C1 and C2 atoms in glycerol correspond to the C4 and S atoms in the C6-CoA adduct, respectively. Under these structural circumstances, His934 is proximal to the hydroxyl group at C4 in the C6-CoA adduct. In fact, His934 is within 3.6 Å from the hydroxyl group at the *pro-S* C1 and C2 carbons of glycerol (Fig. 22, B and C). Moreover, my kinetic analysis indicated a significant role for His934 in catalysis, in particular *kcat*, not *Km* (Table 1). Taken together, His934 could accept a proton from the C4 hydroxyl group of the C6-CoA adduct and then donate a proton back to the sulfur atom of an intermediate (Fig. 25, steps II and III), cleaving the C4-S bond and

producing acetoacetate and CoA.

However, it is unknown whether cleavage of the C2-C3 and C4-S bonds in the C6-CoA adduct are performed in a sequential or concerted manner. In this study, I did not detect any mutant enzymes that liberated only one product, suggesting that these two bonds are likely cleaved in a concerted manner (Fig. 23B).

The crystal structure of Obc1 in its apo form and a glycerol-bound form provides the first structural insights into the second step of oxalogenesis. This study provides insight into an unusual enzymatic feature, the dual catalytic role of the Obc1 C-domain. Specifically, the C-domain has hydrolase activity mediated by a well-known catalytic triad, and lyase activity mediated by a single histidine residue. Given that the overall structural features of the Obc1 C-domain are similar to that of α/β hydrolase containing a catalytic triad, this suggests that the presence of additional lyase activity is an example of divergent evolution. Consistent with this, oxalogenesis in *Burkholderia* species is indispensable for their survival in the stationary phase.

Figure 25. Proposed mechanism for C6-CoA adduct degradation in the active site of the Obc1 C-domain.

It is noteworthy that the *pro-S* C1 and C2 atoms in glycerol could correspond to their positions to C4 and S atoms in the C6-CoA adduct (step I). In brief, catalytic Ser935 performs a nucleophilic attack on the trigonal C2 atom to generate a tetrahedral intermediate (step II). The resulting oxyanion intermediate can be stabilized by positively charged Arg856 and Arg999. I further propose that His934 acts first as a base to deprotonate the hydroxyl group at C4, and subsequently acts as a catalytic acid to cleave the C4-S bond in the adduct, liberating acetoacetate and CoA (step III). The resulting acyl-Obc1 intermediate would be subject to hydrolysis by a water molecule, generating oxalic acid as a product (step IV and V). This final step is a well-known reaction by a catalytic triad in the α/β hydrolase fold.

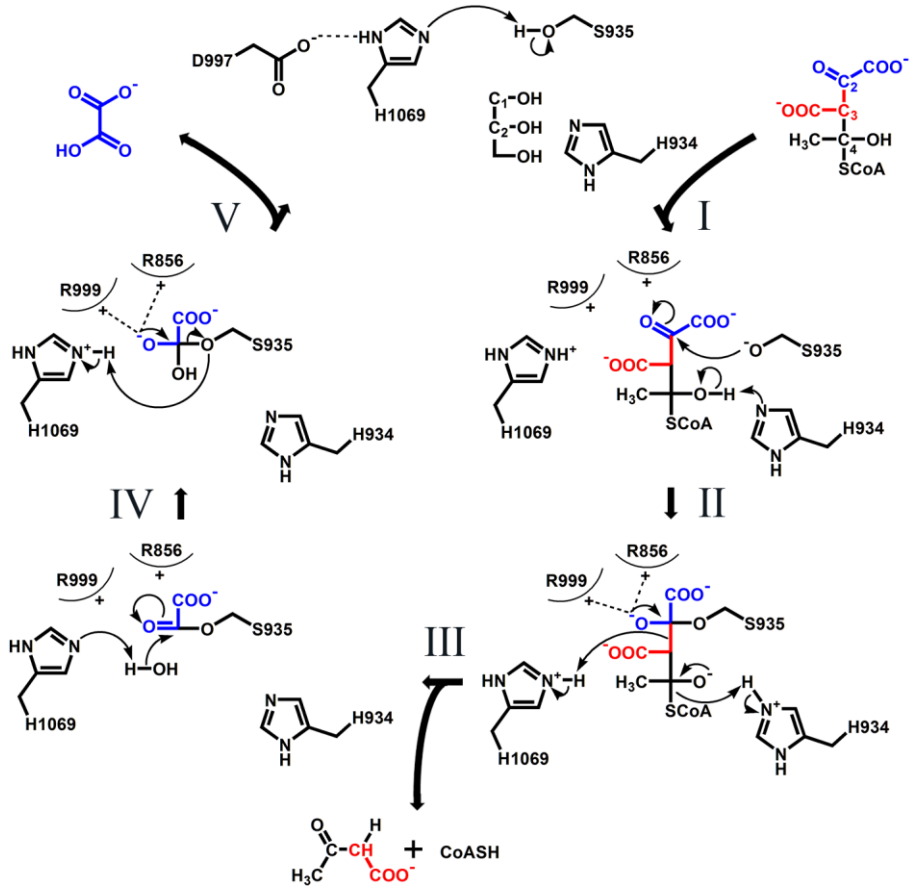
D997
H1069
S935
H934
R856
R999
V
I
IV
II
III
SCoA
CoASH

References

Adams PD, Afonine PV, Bunkoczi G, Chen VB, Davis IW, Echols N et al. (2010) PHENIX: a comprehensive Python-based system for macromolecular structure solution. *Acta Crystallogr D Biol Crystallogr* 66, 213-221.

Battye TG, Kontogiannis L, Johnson O, Powell HR, and Leslie AG (2011) iMOSFLM: a new graphical interface for diffraction-image processing with MOSFLM. *Acta Crystallogr D Biol Crystallogr* 67, 271-281.

Bond CS (2003) TopDraw: a sketchpad for protein structure topology cartoons. *Bioinformatics* 19, 311-312.

Bradley P, Cowen L, Menke M, King J, and Berger B (2001) BETAWRAP: successful prediction of parallel β-helices from primary sequence reveals an association with many microbial pathogens. *Proc Natl Acad Sci USA* 98, 14819-14824.

Buller AR and Townsend CA (2013) Intrinsic evolutionary constraints on protease structure, enzyme acylation, and the identity of the catalytic triad. *Proc Natl Acad Sci USA* 110, E653-661.

Cowtan K (2006) The Buccaneer software for automated model building. 1. Tracing protein chains. *Acta Crystallogr D Biol Crystallogr* 62, 1002-1011.

Dandekar AA, Chugani S, and Greenberg EP (2012) Bacterial quorum sensing and metabolic incentives to cooperate. *Science* 338, 264-266.

Darch SE, West SA, Winzer K, and Diggle SP (2012) Density-dependent fitness benefits in quorum-sensing bacterial populations. *Proc Natl Acad Sci USA* 109, 8259-8263.

Diederichs K and Karplus PA (2013) Better models by discarding data? *Acta Crystallogr D Biol Crystallogr* 69, 1215-1222.

Diggle SP, Griffin AS, Campbell GS, and West SA (2007) Cooperation and conflict in quorum-sensing bacterial populations. *Nature* 450, 411-414.

Dutton MV, and Evans CS (1996) Oxalate production by fungi: its role in pathogenicity and ecology in the soil environment. *Can J Microbiol* 42, 881-895.

Dyda F, Klein DC, and Hickman AB (2000) GCN5-related N-acetyltransferases: a structural overview. *Annu Rev Biophys Biomol Struct* 29, 81-103.

Emsley P, Lohkamp B, Scott WG, and Cowtan K (2010) Features and development of Coot. *Acta Crystallogr D Biol Crystallogr* 66, 486-501.

Evans PR (2011) An introduction to data reduction: space-group determination, scaling and intensity statistics. *Acta Crystallogr D Biol Crystallogr* 67, 282-292.

Eydoux C, Spinelli S, Davis TL, Walker JR, Seitova A, Dhe-Paganon S et al. (2008) Structure of human pancreatic lipase-related protein 2 with the lid in an open conformation. *Biochemistry* 47, 9553-9564.

Franceschi VR and Nakata PA (2005) Calcium oxalate in plants: formation and function. *Annu Rev Plant Biol* 56, 41-71.

Fuqua C and Greenberg EP (2002) Listening in on bacteria: acyl-homoserine lactone signalling. *Nat Rev Mol Cell Biol* 3, 685-695.

Galyov EE, Brett PJ, and DeShazer D (2010) Molecular insights into *Burkholderia pseudomallei* and *Burkholderia mallei* pathogenesis. *Annu Rev Microbiol* 64, 495-517.

Gasteiger E, Gattiker A, Hoogland C, Ivanyi I, Appel RD, and Bairoch A (2003)

ExPASy: The proteomics server for in-depth protein knowledge and analysis. *Nucleic Acids Res* 31, 3784-3788.

Gerlt JA, Babbitt PC, and Rayment I (2005) Divergent evolution in the enolase superfamily: the interplay of mechanism and specificity. *Arch Biochem Biophys* 433, 59-70.

Goo E, An JH, Kang Y, and Hwang I (2015) Control of bacterial metabolism by quorum sensing. *Trends Microbiol* 23, 567-576.

Goo E, Majerczyk CD, An JH, Chandler JR, Seo YS, Ham H et al. (2012) Bacterial quorum sensing, cooperativity, and anticipation of stationary-phase stress. *Proc Natl Acad Sci USA* 109, 19775-19780.

Gouet P, Courcelle E, Stuart DI, and Metoz F (1999) ESPript: analysis of multiple sequence alignments in PostScript. *Bioinformatics* 15, 305-308.

Govindasamy L, Pedersen B, Lian W, Kukar T, Gu Y, Jin S et al. (2004) Structural insights and functional implications of choline acetyltransferase. *J Struct Biol* 148, 226-235.

Ham JH, Melanson RA, and Rush MC (2011) *Burkholderia glumae*: next major pathogen of rice? *Mol Plant Pathol* 12, 329-339.

Heilmann S, Krishna S, and Kerr B (2015) Why do bacteria regulate public goods by quorum sensing?—How the shapes of cost and benefit functions determine the form of optimal regulation. *Front Microbiol* 6, 767

Holm L and Rosenstrom P (2010) Dali server: conservation mapping in 3D. *Nucleic Acids Res* 38, W545-549.

Hoppe B (2012) An update on primary hyperoxaluria. *Nat Rev Nephrol* 8, 467-475.

Jogl G and Tong L (2003) Crystal structure of carnitine acetyltransferase and implications for the catalytic mechanism and fatty acid transport. *Cell* 112, 113-122.

Jones AJ and Hirst J (2013) A spectrophotometric coupled enzyme assay to measure the activity of succinate dehydrogenase. *Anal Biochem* 442, 19-23.

Karplus PA and Diederichs K (2012) Linking crystallographic model and data quality. *Science* 336, 1030-1033.

Keegan RM and Winn MD (2007) Automated search-model discovery and preparation for structure solution by molecular replacement. *Acta Crystallogr D Biol Crystallogr* 63, 447-457.

Kelley LA, Mezulis S, Yates CM, Wass MN, and Sternberg MJ (2015) The Phyre2 web portal for protein modeling, prediction and analysis. *Nat Protoc* 10, 845-858.

Kourist R, Jochens H, Bartsch S, Kuipers R, Padhi SK, Gall M et al. (2010) The α/β-hydrolase fold 3DM database (ABHDB) as a tool for protein engineering. *Chembiochem* 11, 1635-1643.

Lee SG and Jez JM (2013) Evolution of structure and mechanistic divergence in di-domain methyltransferases from nematode phosphocholine biosynthesis. *Structure* 21, 1778-1787.

Lee SG and Jez JM (2014) Nematode phospholipid metabolism: an example of closing the genome-structure-function circle. *Trends Parasitol* 30, 241-250.

Leitao JH, Sousa SA, Ferreira AS, Ramos CG, Silva IN, and Moreira LM (2010) Pathogenicity, virulence factors, and strategies to fight against *Burkholderia cepacia* complex pathogens and related species. *Appl Microbiol Biotechnol* 87, 31-40.

Li HQ, Matsuda I, Fujise Y, and Ichiyama A (1999) Short-chain acyl-CoA-dependent production of oxalate from oxaloacetate by *Burkholderia glumae*, a plant pathogen which causes grain rot and seedling rot of rice via the oxalate production. *J Biochem* 126, 243-253.

Miller MB and Bassler BL (2001) Quorum sensing in bacteria. *Annu Rev Microbiol* 55, 165-199.

Murray IA and Shaw WV (1997) O-Acetyltransferases for chloramphenicol and other natural products. *Antimicrob Agents Chemother* 41, 1-6.

Nakamura H, Mogi Y, Hattori H, Kita Y, Hattori D, Yoshimura A et al. (2008) Absorption-based highly sensitive and reproducible biochemical oxygen demand measurement method for seawater using salt-tolerant yeast *Saccharomyces cerevisiae* ARIF KD-003. *Anal Chim Acta* 620, 127-133.

Nakata PA (2011) The oxalic acid biosynthetic activity of *Burkholderia mallei* is encoded by a single locus. *Microbiol Res* 166, 531-538.

Nakata PA and He C (2010) Oxalic acid biosynthesis is encoded by an operon in *Burkholderia glumae*. *FEMS Microbiol Lett* 304, 177-182.

Nardini M and Dijkstra BW (1999) α/β hydrolase fold enzymes: the family keeps growing. *Curr Opin Struct Biol* 9, 732-737.

Otwinowski Z and Minor W (1997) Processing of X-ray diffraction data. *Methods Enzymol* 276, 307-326.

Pai A, Tanouchi Y, and You L (2012) Optimality and robustness in quorum sensing (QS)-mediated regulation of a costly public good enzyme. *Proc Natl Acad Sci USA* 109, 19810-19815.

Raychaudhuri A, Jerga A, and Tipton PA (2005) Chemical mechanism and substrate specificity of RhlI, an acylhomoserine lactone synthase from *Pseudomonas aeruginosa*. *Biochemistry* 44, 2974-2981.

Robert X and Gouet P (2014) Deciphering key features in protein structures with the new ENDscript server. *Nucleic Acids Res* 42, W320-324.

Sandoz KM, Mitzimberg SM, and Schuster M (2007) Social cheating in *Pseudomonas aeruginosa* quorum sensing. *Proc Natl Acad Sci USA* 104, 15876-15881.

Schuster M, Sexton DJ, Diggle SP, and Greenberg EP (2013) Acyl-homoserine lactone quorum sensing: from evolution to application. *Annu Rev Microbiol* 67, 43-63.

Terwilliger TC (2000) Maximum-likelihood density modification. *Acta Crystallogr D Biol Crystallogr* 56, 965-972.

Terwilliger TC and Berendzen J (1999) Evaluation of macromolecular electron-density map quality using the correlation of local r.m.s. density. *Acta Crystallogr D Biol Crystallogr* 55, 1872-1877.

Walter TS, Meier C, Assenberg R, Au KF, Ren J, Verma A et al. (2006) Lysine methylation as a routine rescue strategy for protein crystallization. *Structure* 14, 1617-1622.

Waters CM and Bassler BL (2005) Quorum sensing: cell-to-cell communication in bacteria. *Annu Rev Cell Dev Biol* 21, 319-346.

Wiegand G and Remington SJ (1986) Citrate synthase: structure, control, and mechanism. *Annu Rev Biophys Biophys Chem* 15, 97-117.

Winn MD, Ballard CC, Cowtan KD, Dodson EJ, Emsley P, Evans PR et al. (2011) Overview of the CCP4 suite and current developments. *Acta Crystallogr D Biol Crystallogr* 67, 235-242.

Yuan H and Marmorstein R (2013) Histone acetyltransferases: Rising ancient counterparts to protein kinases. *Biopolymers* 99, 98-111.

Abstract in Korean

Quorum sensing에 의하여 매개되는 옥살산 생합성은 *Burkholderia*의 정체기 생존에 필수적인 역할을 한다. 생성된 옥살산은 배양 환경의 pH를 유지하는 데에 중심적인 역할을 하는데, 옥살산이 생성되지 않을 경우 아미노산 대사로 인해 생성된 암모니아의 알칼리성 독성에 의해 전체 세균 집단이 붕괴, 사멸된다. 식물 병원성균 *B. glumae*의 경우, 두가지 효소에 의하여 옥살산이 생성된다. 첫 번째 효소는 oxalate biosynthetic component (Obc) A로써 acetyl-CoA와 oxaloacetate를 기질로 이용하여 tetrahedral C6-CoA 부가체를 생성한다. 생성된 부가체는 두 번째 효소인 ObcB에 의하여 oxalic acid, acetoacetate, CoA로 분해된다. 흥미롭게도, *B. thailandensis*와 *B. pseudomallei*의 경우 이러한 두 단계의 반응이 두 효소 기능을 동시에 가지는 Obc1에 의하여 매개된다. Obc1은 N-말단에 ObcA와 서열과 구조가 유사한 도메인을 가지고 있으며, C-말단에 서열은 다르지만 기능은 ObcB와 동일한 도메인을 가지고 있다. 본 학위논문에서는 ObcA와 Obc1의 단백질 결정 구조 및 기능 분석을 통해 옥살산 생합성의 구조적, 기능적 특성을 밝히고자 한다. 먼저 ObcA와 Obc1의 N-말단 도메인은 $(\beta/\alpha)_8$-barrel 접힘 구조를 가지고 있으며, 활성 부위에 금속 이온이 결합되어 있다. 반응 기작의 측면에서는 타이로신 잔기에 의해 활성화된 oxaloacetate가 친핵제로 작용하여 acetyl-CoA의 thioester carbonyl carbon을 공격함으로써 tetrahedral 부가체를 형성한다. CoA가 관여되는 대부분의 tetrahedral 중간체 형성 반응은 음전하의 축적에 의하여 중간체가 붕괴되며, 결과적으로

CoA moiety가 중간체로부터 해리된다. 하지만 ObcA의 경우 이러한 중간체의 붕괴를 야기하는 general acid로 작용할 잔기가 활성부위에 없고, 마그네슘 이온이 coordination shell을 제공하여 tetrahedral CoA 부가체를 안정적인 결과물로 형성하고있다. Obc1의 C-말단 도메인의 경우 catalytic triad를 가지는 α/β hydrolase로 이루어져 있다. 일반적인 α/β hydrolase는 반응 중간체의 불안정한 음전하를 안정화 시켜주는 “oxyanion hole”로써 HGGG motif를 가지고 있는데, Obc1은 이러한 부분에 특이한 구조를 가지고 있다. 또한 단백질 돌연변이를 이용한 기능 분석을 통하여 His934 잔기가 lyase 활성을 가지게 해주는 추가적인 general acid/base로 작용함을 밝혔고, 이를 통해 acetoacetate와 CoA의 형성 메커니즘을 제안하였다. 이러한 결과는 세균의 옥살산 생합성을 구조적, 기능적으로 이해할 수 있는 기반을 제공하며, 이미 단백질 삼차구조가 많이 알려진 α/β hydrolase fold를 구성함에도 불구하고 hydrolase와 lyase 활성을 둘 다 가짐으로써, 환경에서 살아남고 적응하기 위해 기능적 다양성을 가지게 되는 분기진화의 한 예시를 제공한다.

주요어: Quorum sensing, Public goods, Oxalate biosynthetic component, Oxalic acid, Acetyl-CoA, Crystal structure, *Burkholderia* species

학 번: 2010-23457